

## Role of Multiple Charge States of Ce in the Scintillation of $ABO_3$ Perovskites

G. Pilania,<sup>1,\*</sup> S. K. Yadav,<sup>1,†</sup> M. Nikl,<sup>2</sup> B. P. Uberuaga,<sup>1</sup> and C. R. Stanek<sup>1</sup>

<sup>1</sup>*Materials Science and Technology Division, Los Alamos National Laboratory, Los Alamos, New Mexico 87545, USA*

<sup>2</sup>*Institute of Physics, Academy of Sciences of the Czech Republic, 16253 Prague, Czech Republic*

 (Received 11 February 2018; revised manuscript received 20 April 2018; published 20 August 2018)

Ce-activated  $A^{2+}B^{4+}O_3$  perovskites represent a class of compounds currently under active exploration for their potential as scintillators. Depending on the chemistry and synthesis conditions, perovskites can crystallize in multiple crystal structures, and a Ce substitutional dopant in an  $ABO_3$  perovskite can adopt different charge states (i.e.,  $Ce^{3+}$  or  $Ce^{4+}$ ) as well as different substitutional sites (namely, the 12-fold-coordinated  $A$  site or the octahedrally coordinated  $B$  site). Here, we use first-principles density-functional-theory- and hybrid-functional-based computations to study relative trends in the structure, energetics, and electronic structure of bulk  $ABO_3$  perovskites, where  $A = Ca, Sr, \text{ or } Ba$  and  $B = Hf \text{ or } Zr$ . Subsequently, we consider the relative energetics of preferential solution sites for Ce as a function of charge states, chemical potential, and defect configurations. Our results reveal that while  $Ce^{3+}$  or  $Ce^{4+}$  defects can be thermodynamically stable, depending on the choice of the substitutional site and synthesis conditions (i.e., prevailing chemical potential), only  $Ce^{3+}$  dopant at the  $A$  site leads to an electronic structure that can exhibit scintillation. Our comparative analysis shows that while the positions of the  $5d^1$  and  $4f$  levels of  $Ce^{3+}$  as a dopant at the  $A$  site are favorably placed in the band structure, these levels are consistently higher for the  $Ce^{4+}$  charge state and are unlikely to manifest any luminescence. The findings of this study are also discussed in relation to previously reported results and display excellent agreement with past experimental observations. In general, it is demonstrated that control of the Ce charge state and local chemical environment can be used—in addition to band-gap and band-edge engineering—to manipulate the relative position of scintillating states with respect to the valence-band maximum and conduction-band minimum. While this study specifically focuses on perovskites, the results (in particular, the relative alignment of the positions of the  $5d^1$  and  $4f$  levels of Ce dopant as a function of the activator's charge state) are expected to be general and thus transferable to other chemistries.

DOI: [10.1103/PhysRevApplied.10.024026](https://doi.org/10.1103/PhysRevApplied.10.024026)

### I. INTRODUCTION

Scintillators constitute an important class of materials that can efficiently absorb radiation and emit light pulses with a wavelength in or near the visible spectral region [1]. Inorganic scintillators are heavily employed in many fields of applied and fundamental research, including radiation and particle detection in high-energy and astrophysics experiments, medical imaging, oil-well logging, and detection of nuclear materials for homeland security [2–6]. High-quality single crystals (i.e., structurally perfect crystals with very low defect concentrations) of semiconductor or insulator materials are ideally suited for these applications. In addition to a suitable band gap, the materials must exhibit salient electronic structure features

that allow a fast and efficient transformation of incoming high-energy radiation into a number of electron-hole pairs and their subsequent fast radiative recombination after they have been recollected at the conduction-band edge and valence-band edge, respectively [6–8]. In many cases, owing to very high melting temperatures exhibited by these chemistries, synthesis of high-quality single crystals becomes challenging, and therefore other formats, such as transparent polycrystalline ceramics, are sought. While most efforts related to transparent ceramic scintillators have explored binary halides [9–11], garnets [12], and orthosilicates and pyrosilicates [13,14], more recent studies have focused on perovskites [15,16]. In particular, perovskite oxides of the form  $A^{2+}B^{4+}O_3$  with  $A = Ca, Sr, \text{ or } Ba$  and  $B = Zr \text{ or } Hf$  and  $A'^{3+}B'^{3+}O_3$  with  $A' = Y, Gd, \text{ or } Lu$  and  $B' = Al$  doped with Ce as an activator impurity have been investigated because of their excellent gamma-ray attenuation resulting from their high density and high effective atomic number [17–21]. Despite

\*gpilania@gmail.com

†Current address: Metallurgical and Materials Engineering Department, Indian Institute of Technology Madras, Chennai 600036, India

significant efforts, however, only limited success has been achieved in making Ce-doped perovskites scintillating. In most cases no scintillating behavior is reported, and the absence of scintillation is generally attributed to Ce  $5d$  states buried deep in the conduction band, as a result of which excited electrons, after thermally relaxing to the conduction-band edge, fail to localize at the luminescence centers.

More recently, however, a number of studies have reported radioluminescence in BaHfO<sub>3</sub>- and SrHfO<sub>3</sub>-based phosphors and scintillators when they are synthesized in special conditions [22–25]. These investigations have mainly relied on strategies such as (i) co-doping with various charge-compensating metal ions such as Lu, Al, and Ta ions [22] or Li ions [23]; (ii) heavy  $A$ -site doping of Ce in a highly- $A$ -deficient nonstoichiometric perovskite [24], or (iii) synthesis of the compounds in highly reducing conditions [25]. However, the mechanistic details of scintillation in these compounds across diverse chemistries are complicated due to a number of factors and are not yet completely understood. For instance, for a given set of chemistries (i.e., the choice of  $A$  and  $B$  atomic species) and synthesis conditions (e.g., oxidizing or reducing conditions or excess of  $AO$  or  $BO_2$  precursors), a Ce substitutional dopant in an  $ABO_3$  perovskite can adopt different charge states (i.e., Ce<sup>3+</sup> or Ce<sup>4+</sup>) as well as different substitutional sites (i.e., the 12-fold-coordinated  $A$  site or the sixfold-coordinated  $B$  site). The thermodynamics of the dopant formation at different sites in different charge states is primarily governed by the prevailing chemical potential during the synthesis. The details of electronic structure—largely dictating the scintillation performance—are also closely and sensitively tied to the charge states and coordination environment of the activator. A systematic understanding of concerted interplay of these factors not only provides insight into the reported experimental observations but also opens new pathways toward a rational design of targeted functionality in these compounds.

First-principles calculations within the framework of density functional theory (DFT) and “*beyond*” approaches can be particularly useful in studying systematic trends and gaining insights into chemical and electronic properties of materials, and thereby aid the search for better materials or improved modifications of existing materials. Over the past decade, DFT has been extensively employed to study and search for novel and improved rare-earth-doped inorganic scintillator materials and has already significantly contributed to our present understanding of these materials [17,26–34]. The main aim of the present study is to understand trends in the thermodynamic stability of Ce dopants within the perovskite crystal structure across a range of chemistries as a function of Ce charge state, doping site, and synthesis conditions. Once the energetically favorable dopant sites and charge states are identified, the scintillation behavior can be qualitatively understood by

one looking at the relevant electronic-structure features of the most energetically stable dopants. In this direction, here we study the relative thermodynamic stability in different doping situations as a function of chemical potential within the framework of first-principles thermodynamics—an approach that has been extensively employed to study the temperature- and environment-dependent stability of bulk and surface phases within DFT. Further, since a necessary condition for scintillation in Ce-activated materials is that the Ce  $4f$  and  $5d^1$  levels must lie in the forbidden gap of the host material, appropriately situated with respect to the valence-band maximum (VBM) and conduction-band minimum (CBM), our electronic-structure analysis specifically focuses on the Ce  $4f$  and  $5d$  levels relative to the valence-band and conduction-band edges.

A number of studies focused on  $5d$ - $4f$  transitions for a range of lanthanide activators using band-structure calculations [32–37]. A general consensus appears to be that for conventional local and semilocal exchange-correlation functionals within DFT, such as the local-density approximation (LDA) or the generalized gradient approximation (GGA), the self-interaction error associated with the localized nature of the  $4f$  electrons prohibits the calculation of accurate energy differences as well as the location of the energy bands. There have been attempts to overcome this problem either by use of methods that go beyond DFT [30,33] or by electronic-structure calculations with the LDA+U or GGA+U approach [38,39] to get a better description of the localized  $4f$  states of Ce compared with that obtained with the LDA or GGA [32,34,37]. However, it is needless to emphasize that care should be taken while one is approximating the exact  $4f$ - $5d$  excitation energies by the one-electron energies within the DFT framework. Using a combination of the pseudopotential plane-wave method along with the relativistic molecular-orbital approach, Watanabe and Ogasawara [40] studied the  $4f$ - $5d$  absorption spectra of Ce-doped LiYF<sub>4</sub>. They concluded that owing to the simple [Xe] $4f^1$  electronic structure of Ce<sup>3+</sup>, the  $4f$ - $5d$  transitions can indeed be attributed to transitions between molecular orbitals, and therefore can be analyzed within the framework of a single-electron approximation.

In the present study, we employ the hybrid Heyd-Scuseria-Ernzerhof (HSE) [41,42] functionals that are built from the Perdew-Burke-Ernzerhof (PBE) [43] GGA functional by replacement of a fraction  $\alpha$  of the semilocal PBE exchange interaction by a screened nonlocal functional (with a second parameter  $\omega$  representing the inverse screening length) to investigate the electronic structure of bulk and Ce-doped  $ABO_3$  perovskites, where  $A = \text{Ca, Sr, or Ba}$  and  $B = \text{Hf or Zr}$ . We find that the standard HSE06 functional (where the tuple  $\{\alpha, \omega\}$  maps onto  $\{0.25, 0.207 \text{ \AA}^{-1}\}$ ) [44], although giving a substantial improvement over the PBE results, still significantly underestimates

the bulk band gaps of the perovskite compounds. Further increasing  $\alpha$  systematically leads to wider band gaps. We show that tuning of  $\alpha$  to reproduce the correct experimental band gap for one of the bulk compounds not only reproduces the bulk band gaps of the rest of the compounds to good accuracy but also provides a correct description of their relative valence-band and conduction-band alignments. This hybrid functional is subsequently used to compute the electronic structure of Ce-doped supercells.

To summarize our results, our chemical-potential-dependent dopant formation energies indicate that, depending on the experimental synthesis conditions, a Ce impurity can occupy substitutional sites at either  $A$  or  $B$  sublattices with  $3+$  and  $4+$  charge states, respectively. Substitutions with  $\text{Ce}^{3+}$  at the  $B$  site and  $\text{Ce}^{4+}$  at the  $A$  site consistently lead to higher formation energies, irrespective of the host chemistry. Furthermore, the  $A$ -site-substituted  $\text{Ce}^{3+}$  impurity is predicted to exhibit a scintillating behavior, while for the  $\text{Ce}^{4+}$  case,  $\text{Ce } 5d$  states always appear deep in the conduction band. Finally, consistent with the experimental observations, we predict that for both  $AO$ -deficient and highly reducing conditions, the  $A$ -site-substituted  $\text{Ce}^{3+}$  impurity is thermodynamically favorable as compared with the  $\text{Ce}^{4+}$  substitution at the  $B$  site, rationalizing the observed scintillating behavior in these specific situations. In what follows, we describe our findings in greater detail.

## II. TECHNICAL DETAILS

DFT calculations are performed with the VIENNA AB INITIO SIMULATION PACKAGE (VASP) [45,46]. Unless mentioned otherwise, the DFT calculations employ the PBE [43] GGA exchange-correlation functional. The electronic wave functions are expanded in plane waves up to a cut-off energy of 500 eV. The pseudopotentials based on the projector-augmented-wave method [47] explicitly include the following valence electronic configurations for different elemental species:  $5s^2 5p^6 6s^2 4f^1 5d^1$  for Ce,  $3s^2 3p^6 4s^2$  for Ca,  $4s^2 4p^6 5s^2$  for Sr,  $5s^2 5p^6 6s^2$  for Ba,  $4p^6 4d^2 5s^2$  for Zr,  $5p^6 5d^2 6s^2$  for Hf, and  $2s^2 2p^4$  for O. It is important to include the  $4f$  shell as part of the Ce valence electronic configuration to allow for the  $3+$  charge state. A  $\Gamma$ -centered automatically generated  $4 \times 4 \times 3$  Monkhorst-Pack  $k$ -point mesh [48] is used for Brillouin-zone integrations for a  $\sqrt{2} \times \sqrt{2} \times 2$  cubic (or pseudocubic in the case of the orthorhombic space group  $Pnma$ ) supercell containing 20 atoms. For smaller or larger supercells, the  $k$ -point meshes are appropriately scaled to give the same  $k$ -point density in the reciprocal space. Spin-polarized calculations are employed for supercells containing unpaired electrons. To obtain a geometry-optimized equilibrium structure, atomic positions and the supercell lattice parameters are fully relaxed with use of the conjugate-gradient method until all the Hellmann-Feynman forces and the

stress component are less than  $0.01 \text{ V/\AA}$  and  $1.0 \times 10^{-2} \text{ GPa}$ , respectively.

Sufficiently large supercells, containing 160 atoms, are consistently used to model the defect configurations. In the defect calculations, the dimensions of the supercells are always fixed to the corresponding relaxed bulk lattice parameters, while all the internal degrees of freedom are allowed to relax. To model isolated Ce dopants in different charge states, electrons are adequately added to or removed from the supercell and a compensating background charge density is added. Spurious electrostatic interactions of charged defects due to periodicity and finite supercell sizes are accounted for by first-order monopole corrections [49].

Since conventional local and semilocal exchange-correlation functionals, including the PBE functional, significantly underestimate the electronic band gap, the HSE functional is used on the relaxed PBE geometries to obtain an improved description of the band gap and the activator's  $4f$  and  $5d^1$  levels. The hybrid-density-functional methods have been shown to improve results for the band gap and charge localization in semiconductors and insulators [50–52]. However, we also note that for metallic systems the hybrid functionals are not suitable and have been reported to significantly overestimate bandwidths and exchange splitting [50].

Within this family of functionals, one has access to the parameters  $\alpha$  and  $\omega$ , representing the fraction of exact exchange and the inverse screening length, respectively, which can be used to tune the details of the electronic structure within a given class of materials. In particular, tuning of band gaps, band edges, and defect levels has been studied in detail [53]. For specific choices of the parameters  $\{\alpha, \omega\}$  the standard functionals, such as the PBE  $\{\alpha = 0\}$ , PBE0  $\{\alpha = 0.25, \omega = 0\}$ , and HSE06  $\{\alpha = 0.25, \omega = 0.207 \text{ \AA}^{-1}\}$  functionals can be obtained from the family of hybrid functionals. Komsa *et al.* [53] studied details of tuning the band gap by varying  $\alpha$  in PBE0-like (i.e.,  $\omega$  fixed at 0) and in HSE-like (i.e.,  $\omega$  fixed at  $0.207 \text{ \AA}^{-1}$ ) hybrid functionals. Their results show that for PBE0-like functionals the band gap increases linearly with the fraction of exact exchange  $\alpha$ , which is also in agreement with other reports [54,55]. For HSE-like functionals, slight deviations from linear behavior are observed, and the change in the band gap with  $\alpha$  occurs at a smaller rate. Going to nonstandard hybrid functionals by further decreasing the screening lengths (i.e., larger  $\omega$ ) requires an increasingly large fraction of exact exchange to reach a given value of the band gap. However, such large values of  $\alpha$  eventually lead to a poor description of energetics [41,44]. It is also found that when the band gap is tuned by varying  $\alpha$ , the PBE0 and HSE functionals both yield nearly identical results for defect-level positions in the band gap and for band offsets at interfaces. Following this approach, here we vary the amount of exact exchange  $\alpha$  within the HSE-like functionals to tune the band gaps in the perovskite compounds. As

mentioned briefly in Sec. I, we find that while the standard HSE06 functional [44] with  $\alpha = 0.25$  and  $\omega = 0.207 \text{ \AA}^{-1}$  underestimates the band gaps as compared with experiments, further increasing  $\alpha$  to 0.4 and keeping the inverse screening length fixed to that of the standard HSE06 functional accurately reproduces the experimental band gaps and the relative alignments of the band edges for the bulk compounds studied here. The HSE functional with  $\alpha = 0.4$  is subsequently used to study the electronic structure of the Ce-doped compounds.

### III. RESULTS

#### A. Bulk properties

Although the general focus of this work is the electronic structure and energetics of  $\text{Ce}^{3+}$ - or  $\text{Ce}^{4+}$ -doped  $A^{2+}B^{4+}\text{O}_3$  perovskites with  $A = \text{Ca, Sr, or Ba}$  and  $B = \text{Hf or Zr}$ , there are noteworthy structural differences and chemical trends among the bulk compounds considered. From a scintillation point of view, while the  $A^{2+}B^{4+}\text{O}_3$  perovskite host compounds studied here consistently show high stopping power (owing to the high nuclear charge) and high melting temperatures, there are also trade-offs in certain structure-property relationships exhibited by these compounds. For instance, both  $\text{BaHfO}_3$  and  $\text{BaZrO}_3$  adopt cubic crystal structures with indirect band gaps, whereas the other four compounds, with Ca and Sr at the  $A$  site, are orthorhombic direct-band-gap insulators. Note, however, that a cubic material with a direct band gap is ideally suitable as a scintillator host since with noncubic materials it is relatively difficult to produce large transparent ceramics at low cost owing to their highly anisotropic nature. However, energy transfer from the VBM to the CBM has to be mediated with phonons in the case of an indirect-band-gap material, typical of the cubic materials. Therefore, before presenting our results on charge-state- and chemical-potential-dependent Ce-dopant formation energies and substitutional-site-dependent (i.e.,  $A$ - or  $B$ -site-dependent) electronic structure, we briefly discuss the structure, energetics, and chemical trends in the band gap and band edges of bulk  $A^{2+}B^{4+}\text{O}_3$  compounds.

The main structural distinction among the class of compounds considered is that, as already alluded to, the compounds comprising Ba at the  $A$  site are cubic and crystallize in the  $Pm\bar{3}m$  space group (no. 221) [56], while those with Ca or Sr at the  $A$  site display an orthorhombic crystal structure with space group  $Pnma$  (no. 62) [57] owing to an energetically favored pattern of  $\text{BO}_6$  octahedral rotations (i.e., the  $a^-b^+a^-$  tilt pattern configuration according to Glazer's notation) [58]. These local rotational distortions are driven by the difference in ionic radius between  $A^{2+}$  and  $B^{4+}$  cationic species, and are generally described by the well-known Goldschmidt *tolerance factor* ( $t$ ), which aims to capture deviation from an idealized packing of cations and anions in the  $AO$  and  $BO_2$  [001] planes in

the structure [59]. The situation with  $t = 1$  corresponds to an ideal perovskite, while a decreasing  $t$  corresponds to an increasing degree of distortion. The compounds considered in this study adhere to standard tolerance-factor guidelines; that is, if the tolerance factor of a compound is near unity, that compound should be cubic (as is the case for  $\text{BaHfO}_3$  and  $\text{BaZrO}_3$ , with  $t = 1.009$  and  $1.004$ , respectively), and as the tolerance factor decreases, the tendency for orthorhombic distortions to occur increases systematically [57,60,61].

To quantify the relative tendency for different chemistries to adopt a cubic versus an orthorhombic structure, we report the relative formation energy of the two phases as a function of  $A$ - and  $B$ -site chemistry in Fig. 1(a). To better capture the chemical trends in energetics and electronic structure, in addition to the six bulk  $ABO_3$  single perovskites, we also include chemistries formed by a 50% admixture of rock-salt-ordered  $A$ - and/or  $B$ -site cation pairs appearing as nearest neighbors in different columns of the periodic table. As can be seen from Fig. 1(a), all compounds with Ba as the  $A$ -site cation as well as  $\text{Ba}_{0.5}\text{Sr}_{0.5}\text{HfO}_3$  prefer the cubic  $Pm\bar{3}m$  structure over the orthorhombic  $Pnma$  structure. As one moves to chemistries that exhibit a smaller average  $A$ -site cation radius (going from Ba to Ca) and/or a larger average  $B$ -site cation radius (i.e., going from Hf to Zr; note that the octahedrally coordinated  $\text{Zr}^{4+}$  has a larger ionic radius than  $\text{Hf}^{4+}$ ), the tendency for the  $B$ -site octahedral rotations increases, and as a result, the orthorhombic crystal structure increasingly becomes more energetically favored. The relaxed lattice parameters for the bulk compounds in their respective ground-state crystal structures are provided in Table I and are compared with available experimentally obtained values. A systematic overestimation of the structural parameters can be attributed to the tendency for a slight underbinding in the PBE functional, or in general for all GGA functionals, within DFT.

In addition to the relative formation energies between the cubic and orthorhombic phases, Fig. 1(b) reports the formation energies of the perovskite compounds (computed in the most stable crystal structure, i.e.,  $Pnma$  or  $Pm\bar{3}m$ ) with respect to the corresponding  $AO$  (viz.,  $\text{CaO}$  [69],  $\text{SrO}$  [70], and  $\text{BaO}$  [71] in the rock-salt  $Fm\bar{3}m$  crystal structure) and  $BO_2$  (viz.,  $\text{ZrO}_2$  [72] and  $\text{HfO}_2$  [73] in the monoclinic  $P2_1/c$  crystal structure) binary phases. It is interesting to note the correlation between the relative energies in Fig. 1(a) and the formation energies in Fig. 1(b), indicating that the larger the deviation from an idealized packing of cations and anions, the greater the extent of octahedral distortions to accommodate the size mismatch between the  $A$ - and  $B$ -site cations and the less stable the compound with respect to its binary constituents.

The correlation between the energies in Figs. 1(a) and 1(b) can also be understood by noting that the enthalpy of formation of a ternary oxide from the

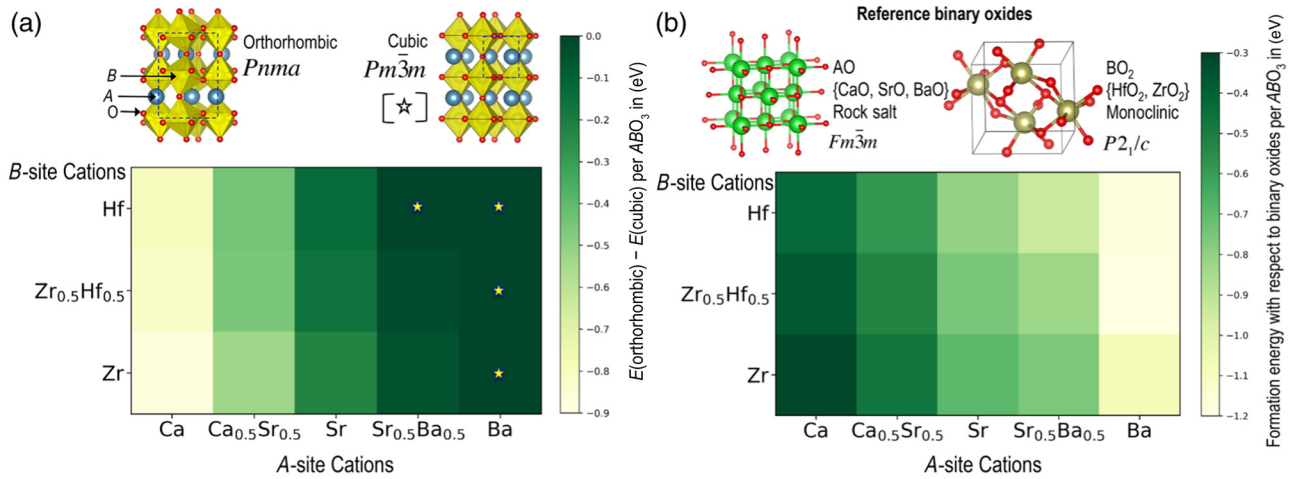


FIG. 1. (a) DFT energies per  $ABO_3$  unit for different chemistries in the orthorhombic  $Pnma$  structure computed relative to the the cubic  $Pm\bar{3}m$  structure reported as a function of  $A$ - and  $B$ -site chemistry. The two structures are also depicted on top of the matrix plot. The compounds that adopt the cubic  $Pm\bar{3}m$  structure as the ground state are indicated with a star. (b) DFT formation energies of the  $ABO_3$  perovskites computed for the most stable crystal structure identified in (a)—that is, using either  $Pnma$  or  $Pm\bar{3}m$ —computed with respect to the corresponding ground-state rock salt  $AO$  (space group  $Fm\bar{3}m$ ) and monoclinic  $BO_2$  (space group  $P2_1/c$ ) binary oxide phases. The unit cells used for the reference binary phases are presented at the top of the panel.

binary constituent oxides can generally be interpreted in terms of factors related to electron transfer between the two oxides, which in turn depend on the basic/acidic nature (or donor/acceptor quality) of the binary oxides. The larger the difference in acidity/basicity of  $AO$  and  $BO_2$  is, the more exothermic the formation enthalpy

becomes. While alkaline-earth-metal oxides are usually basic, transition-metal oxides are acidic, and the basicity increases as one goes down a specific group; for instance, as  $CaO < SrO < BaO$  (as the atomic radius of the metal ion increases). Note, however, again the exception due to the lanthanide contraction, which leads to a larger ionic

TABLE I. DFT-computed relative energies (energies computed in the orthorhombic  $Pnma$  structure relative to the the cubic  $Pm\bar{3}m$  structure), formation energies, relaxed bulk lattice parameters in the ground-state structure, and band gaps computed at different levels of theory for the six  $ABO_3$  single perovskites studied here. Reported experimental values for the lattice parameters and the band gaps are also provided for comparison.

$ABO_3$ compound	Space group	$E_{Pnma} - E_{Pm\bar{3}m}$ (eV/ $ABO_3$ )	$\Delta E_f$ (eV/ $ABO_3$ )	Lattice parameters ( $\text{\AA}$ )			Band gap (eV)				
				PBE	HSE06	HSE $_{\alpha=0.4}$	$G_0W_0$	Expt.			
CaZrO <sub>3</sub>	$Pnma$	-0.873	-0.312	5.62 (5.59) <sup>b</sup>	5.78 (5.76) <sup>b</sup>	8.06 (8.02) <sup>b</sup>	3.99	5.60	6.64	5.97	(6.40) <sup>a</sup>
SrZrO <sub>3</sub>	$Pnma$	-0.223	-0.693	5.80 (5.79) <sup>c</sup>	5.87 (5.82) <sup>c</sup>	8.25 (8.20) <sup>c</sup>	3.72	5.27	6.27	5.63	(6.15) <sup>a</sup>
BaZrO <sub>3</sub>	$Pm\bar{3}m$	0.000	-1.075	4.23 (4.19) <sup>d</sup>			3.14	4.63	5.57	4.68	(5.30) <sup>e</sup>
CaHfO <sub>3</sub>	$Pnma$	-0.791	-0.424	5.60 (5.57) <sup>f</sup>	5.76 (5.73) <sup>f</sup>	8.02 (7.98) <sup>f</sup>	4.49	6.09	7.12	6.47	(6.75) <sup>a</sup>
SrHfO <sub>3</sub>	$Pnma$	-0.130	-0.808	5.76 (5.78) <sup>f</sup>	5.84 (5.80) <sup>f</sup>	8.21 (8.18) <sup>f</sup>	4.17	5.72	6.72	5.98	(6.60) <sup>a</sup> (6.50) <sup>g</sup>
BaHfO <sub>3</sub>	$Pm\bar{3}m$	0.000	-1.180	4.20 (4.18) <sup>f</sup>			3.54	5.04	5.99	5.33	(6.00) <sup>h</sup>

<sup>a</sup>Experimental band gaps based on spectroscopic data combined with estimated exciton binding energies reported in Ref. [65].

<sup>b</sup>Experimental lattice parameters from Ref. [62].

<sup>c</sup>Experimental lattice parameters from Ref. [63].

<sup>d</sup>Experimental lattice parameters from Ref. [64].

<sup>e</sup>Experimental band gaps from Ref. [66].

<sup>f</sup>Experimental lattice parameters from Ref. [60].

<sup>g</sup>Experimental band gaps from Ref. [67].

<sup>h</sup>Experimental band gaps from Ref. [68].

radius for Zr than Hf and therefore renders  $\text{ZrO}_2$  slightly more basic than  $\text{HfO}_2$ . In agreement with these general arguments, the energies of formation of the ternary barium oxides (from their binary constituents) are more negative than those of the corresponding strontium oxides, which are more negative than those of the calcium oxides. Also, for any given *A*-site cation, the formation energies of the ternary hafnates are more negative than those of the zirconates. Further, this trend between the acidity/basicity and the atomic radii of the metal cations is directly responsible for the observed correlation between the energies reported in Figs. 1(a) and 1(b), via the Goldschmidt tolerance factor, as discussed earlier. We also note that the formation energies computed in this study are in good agreement with previously reported experimental [74–76] and theoretical [77,78] results. The computed energies are provided in Table I.

Next we discuss the electronic structure, band gaps, and relative band-edge positions of the bulk compounds. In agreement with previous reports, the electronic band structure and density of states of the  $\text{ABO}_3$  compounds reveal that the valence bands are mainly constituted by O  $2p$  orbitals, while the *B* atoms'  $d$  orbitals largely contribute to the conduction bands. Those compounds stable in the cubic phase exhibit an indirect band gap (with the VBM and CBM lying at the R-point and  $\Gamma$ -point, respectively), while those stable in the orthorhombic phase have a direct band gap at the  $\Gamma$ -point, and this again is in agreement with previous findings. While the relative chemical trends in the band gaps are expected to be correct with use of the PBE functional, the actual band gaps are grossly underestimated as compared with the experimentally measured ones. This tendency is well known for the local and semilocal exchange-correlation functional within DFT (including the PBE functional employed here) and has been attributed to the inherent lack of derivative discontinuity [79] and delocalization error [80,81] within the local or semilocal exchange-correlation functionals [82].

To obtain better predictions of the band gaps, we resorted to more accurate (and also much more computationally expensive) methods; namely, the hybrid HSE06 functional and single-shot quasiparticle  $GW$  (i.e.,  $G_0W_0$ ) [83] calculations on top of the relaxed PBE geometry and PBE eigenfunctions. Figure 2(a) compares our results for the band gaps computed with the PBE and HSE06 functionals for the bulk perovskites in their respective ground-state crystal structures. The band gaps computed with the semilocal and hybrid exchange-correlation functionals exhibit a very similar trend. The HSE06 band gaps can simply be given by a linear function of the PBE band gaps  $\epsilon^{\text{PBE}}$  as  $1.085\epsilon^{\text{PBE}} + 1.2215$  to very good accuracy (with a goodness of fit  $R^2 = 0.997$ ). Nevertheless, comparison with corresponding experimental values (see Table I) reveals that the HSE06 band gaps—although representing a significant improvement as compared with the PBE band

gaps—are still considerably underestimated. The band gaps obtained with the  $G_0W_0$  calculations provide further improvements over the HSE06 values; however, they are still systematically lower than the experimental values, as can be seen from Fig. 2 and Table I. We also find that the relative trends that we see here for the HSE06 and  $G_0W_0$  band-gap calculations (with respect to experiments) are quite general and have also been reported for other wide-band-gap materials [84,85].

It has also been demonstrated that going beyond the single-shot  $GW$  method, via use of the  $GW_0$  approach, further improves the band-gap predictions [85]. In the  $GW_0$  approach, the eigenvalues in the Green's function  $G$  are updated, whereas the screening properties are calculated in the random-phase approximation with use of only the PBE wave functions and eigenvalues. While accurate, this strategy is significantly more computationally expensive and not practical for large supercells containing defects/dopants. Alternatively, we explored a more *pragmatic* strategy, where we systematically vary the fraction of the Hartree-Fock exact exchange  $\alpha$  in the DFT hybrid functional (while fixing the inverse screening length  $\omega$  at the standard HSE06 value) to track the corresponding variation in the band gap. Figure 2(b) presents our results for  $\text{BaHfO}_3$ , where  $\alpha = 0.4$  reproduces the experimental band gap. More interestingly, the bulk band gaps computed with the HSE functional with  $\alpha = 0.4$  for the rest of the compounds result in excellent agreement with the corresponding experimental band gaps at a much lower computational cost than with the  $GW$  approach. In what follows, we consistently used the HSE functional with  $\alpha = 0.4$  to study the electronic structure of the Ce-doped perovskites, as discussed in Sec. III C.

Finally, we note that within our hybrid-functional approach, previously reported relative chemical trends for the valence- and conduction-band edges are also well captured [65]. To reliably determine the relative position of band edges in compounds, a reference state that does not change with chemical composition first needs to be identified. While there are several schemes available in the literature [31,86–89], we use the binding energy of oxygen  $1s$  core electrons to calculate the relative positions of the valence-band and conduction-band edges. An experimentally reported value of the valence-band edge for  $\text{BaZrO}_3$  with respect to the vacuum level from Ref. [65] then allows us to pin the zero of energy. The binding energy of the oxygen  $1s$  core electrons is calculated as the energy difference between two separate calculations [90,91]. The first calculation is a standard DFT calculation in which the number of core electrons corresponds to the ground state, whereas for the second calculation one electron is removed from the core of one particular atom and added to the valence or conduction band. The energy difference then provides the core-level binding energy. Note that the core-electron

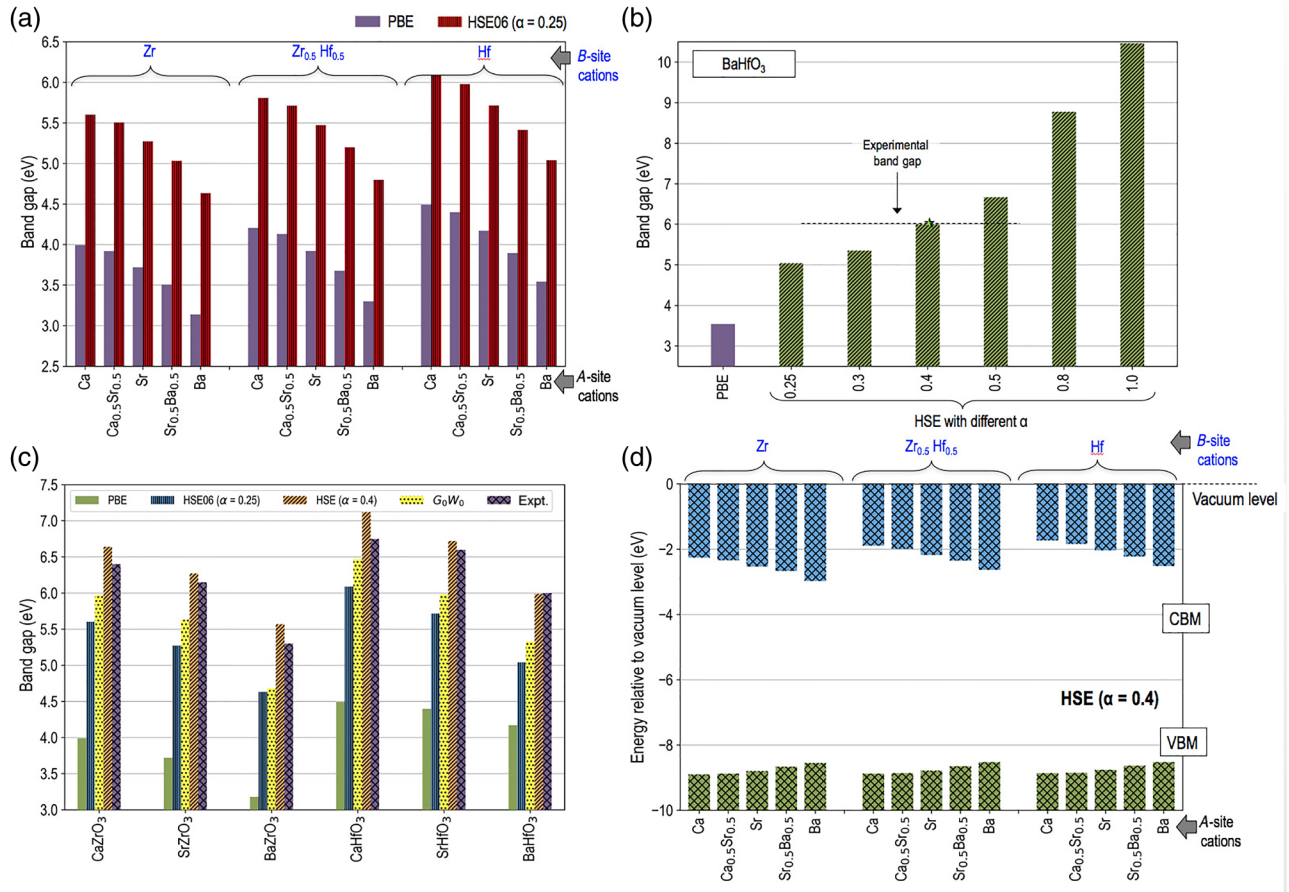


FIG. 2. (a) Band gaps computed with the PBE and HSE06 functionals for the bulk single and double perovskites in their respective ground-state crystal structures. Clear trends in the computed band gaps as a function of *A*- and *B*-site chemistries can be seen. (b) Tuning of the band gap for the cubic perovskite  $BaHfO_3$  by systematic variation of the fraction of exact exchange  $\alpha$  in the HSE hybrid functional. The experimental value of the band gap, indicated by the horizontal dashed line, is achieved at  $\alpha = 0.4$ . The corresponding PBE value is also shown for comparison. (c) Comparison of the band gaps for the ground-state structures of the six single  $ABO_3$  perovskite chemistries computed at different levels of theories employed in this study and corresponding experimentally reported values in the literature. (d) Relative valence- and conduction-band-edge alignments for the perovskites computed with the HSE hybrid functional with  $\alpha = 0.4$  as a function of *A*- and *B*-site chemistries. The zero of the energy corresponds to the vacuum level. The O 1s core levels are used to align the band edges relative to each other.

binding energies can be calculated with either the initial-state approximation or the final-state approximation. In the final-state approximation the electrons are allowed to relax after the core electron has been removed, so that the acquired localized hole is screened. In the initial-state approximation, on the other hand, the core electron is removed but no change of the potential (e.g., by relaxation of other electrons) is allowed, and electronic screening is therefore entirely ignored. The oxygen core 1s level, however, is sufficiently deep, and we do not expect the predicted values from the two approximations to differ considerably. Further, since the core-electron binding energy in the initial-state approximation can be calculated directly from the Kohn-Sham eigenvalues of the core states and the Fermi level, this approximation is used here to compute the

oxygen 1s core levels. We also note here that the 2s state of oxygen was previously used as a reference to align band edges in garnets [31]. With the deep core state identified, the band edges of the bulk perovskites can then be compared directly by the shifting of the band structure of one of them with respect to the others such that the deep state energy levels coincide across chemistries.

Figure 2(d) presents our results on the relative conduction- and valence-band-edge alignments for different chemistries in a stacked-band scheme. It can be seen in Fig. 2(d) that there are systematic variations in the relative band-edge alignments, which closely follow chemical trends in the periodic table. As we go down group 2 of the periodic table (from Ca to Ba), the atomic size and the metallic nature increase and the band gap systematically

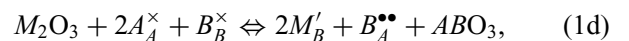
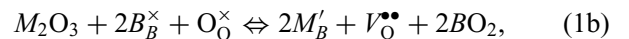
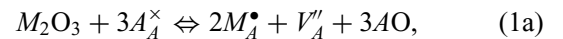
decreases. Both the lowering of the CBM and the rise of the VBM contribute to the band-gap reduction, although the changes in the CBM position are greater than those in the VBM position. Unlike the *A*-site atomic species, Zr and Hf have very similar atomic radii and chemical nature, and as a result, only relatively small changes in the band-edge alignment with respect to the *B*-site atomic species are evident. Finally, we note that the computed trends are in close agreement with experimental observations [65].

### B. Charge-state- and chemical-potential-dependent defect energetics

The  $A^{2+}B^{4+}O_3$  perovskites explored here typically display high melting points and are also frequently employed in formats other than single crystals, such as transparent polycrystalline ceramics [25,92] and nanocrystals [23,93]. While a range of intrinsic defects (such as cation antisite and anion vacancies)—as dictated by thermodynamics at finite temperatures—can naturally occur in these materials, extrinsic defects can also be formed; for instance, via nonstoichiometry or from aliovalent activators through charge compensation (e.g., in the case of  $Ce^{3+}$ ). The presence of defects can have a strong effect on the underlying electronic structure, including the features that are critical to scintillation performance. For instance, in the Ce-activated  $BaHfO_3$  ceramics, a strong influence of the preparation atmosphere (reducing, oxidizing, or inert) on the scintillation efficiency has been reported [25]. Also, contrary to the conventional belief that  $SrHfO_3$  is a line compound in the composition-temperature phase diagram, a small nonstoichiometry in terms of Zr excess has been reported [94], and Sr vacancies have been proposed as defects related to  $SrHfO_3$  nonstoichiometry [24]. Nikl *et al.* [24] recently synthesized heavily-Ce-doped  $SrHfO_3$  and undoped nonstoichiometric  $SrHfO_3$ . They not only found a new emission band at about 334 nm in the Sr-deficient sample but also demonstrated a room-temperature decay time of about 180 ns and efficient and fast energy transfer from the host to the center of the 334-nm emission. Loureiro *et al.* [22] synthesized Ce-activated  $BaHfO_3$  and  $SrHfO_3$  perovskites with different charge-compensating co-dopants. They found that  $Ce^{3+}$  doping at the *A* site is much easier in  $SrHfO_3$  than in  $BaHfO_3$ . High  $Ce^{3+}$  doping concentrations in a  $BaHfO_3$  host lattice were stabilized only at very high temperatures and in reducing conditions, whereas for  $SrHfO_3$  it was found that higher relative percentages of  $Ce^{3+}$  at the Sr site could be obtained with much milder conditions. In addition, the site preference of lanthanide activators has important optical-property implications, as charge transfer is reduced with increase of both the nearest-neighbor distance between the activator and oxygen ions [95] and the coordination number [96]. The site preferences of  $Tm^{3+}$  in  $SrHfO_3$  [97], Eu in  $BaHfO_3$  [98], and Eu in  $SrZrO_3$  nanophosphors [99] have been examined.

In addition to the conventional  $Ce^{3+}$  centers, an exciting avenue is presented by recent developments in scintillation performance improvement by luminescent  $Ce^{4+}$  centers in Ce-doped oxides, in particular garnets [30,100,101] and orthosilicates [102]. A  $Ce^{4+}$  center, if stable in these oxides, can provide an additional fast radiative recombination pathway since it can efficiently compete with any electron traps for immediate capture of electrons from the conduction band. In contrast, a  $Ce^{3+}$  center is much less effective in this competition since it first needs to capture a hole from the valence band to be able to capture an electron in a subsequent step. Also note that scintillation through  $Ce^{3+}$  and  $Ce^{4+}$  centers in a material can, in principle, work in parallel, and therefore the two centers do not compete with each other but rather complement each other. As a result, the presence of stable  $Ce^{4+}$  centers, with appropriately placed electronic levels in the host band gap, can positively influence several scintillation characteristics, including light yield, speed of scintillation response, and afterglow. Acceleration of scintillation response in  $Lu_3Al_5O_{12}:Ce$  and  $Lu_{1.95}Y_{0.05}SiO_5:Ce$  co-doped with alkaline earth metals has been attributed to the presence of  $Ce^{4+}$  centers in recent reports [30,100–102].

Casillas-Trujillo *et al.* [17] reported a systematic study of defect chemistry in  $A^{2+}B^{4+}O_3$  perovskites (with  $A^{2+} = Ba^{2+}$  or  $Sr^{2+}$ , and  $B^{4+} = Zr^{4+}$  or  $Hf^{4+}$ ) employing both atomistic calculations using potentials and DFT computations. This study examined a range of intrinsic defect reactions, several situations with *A*- and *B*-excess nonstoichiometry, and a number of possible reactions for  $M^{3+}$  rare-earth-cation doping ( $Lu^{3+}$  to  $La^{3+}$ ). While for the stoichiometric cases a Schottky disorder was predicted to be the lowest-energy intrinsic process, for nonstoichiometric situations with *AO* excess ( $BO_2$  excess) a charge-compensation mechanism by oxygen vacancies (by *A* vacancies) was found to be the most energetically favored. For the  $M^{3+}$ -dopant formation energies, the following specific reactions were considered (the Kröger–Vink notation is used [103]):

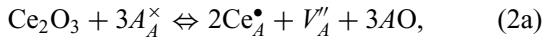


While some of these reactions have been considered by others [104], this comprehensive investigation shows that

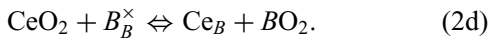
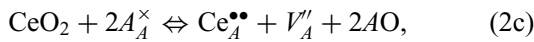
not only the preferred reaction sensitively depends on the specific  $M^{3+}$  dopant being considered but also that the formation energies can differ by several electronvolts across these reactions for a given dopant. For  $Ce^{3+}$ -doping cases, however, the  $A$  site is consistently favored for the entire set of compounds, with the reaction in Eq. (1a) being the most energetically favored route.

Despite all of these studies, there are a number of questions—with particular relevance for scintillators—that remain to be answered regarding Ce doping in  $ABO_3$  perovskites. In particular, questions such as “What is the site preference and dopant formation energy for the  $Ce^{4+}$  charge state?” and “How does it compare with that of the  $Ce^{3+}$  charge state?” remain to be answered. Also, perhaps more importantly, how these formation energies and site preferences change with respect to the chemical environment (i.e., with systematic variation of the chemical potential) has not been addressed. In the remainder of this section, we address these issues in a systematic manner and interpret available experimental observations in light of our computational results.

Building on previous work [17], here we consider the most stable reactions found for  $Ce^{3+}$  doping at the  $A$  site and at the  $B$  site. In addition, we also consider two analogous reactions for  $Ce^{4+}$  doping. For  $Ce^{3+}$  doping at the  $A$  and  $B$  crystal sites, we have



For  $Ce^{4+}$  doping at the  $A$  and  $B$  crystal sites, we have



Note that either bulk  $AO$  or bulk  $BO_2$  appears in each of the reactions in Eqs. (2a)–(2d). While it is common practice to use respective bulk enthalpies (or DFT total energies) as chemical potentials (i.e.,  $\mu_{AO} = E_{AO}^{\text{bulk}}$  and  $\mu_{BO_2} = E_{BO_2}^{\text{bulk}}$ ) to evaluate defect formation energies at 0 K, the thermodynamic equilibrium conditions during the  $ABO_3$  bulk formation strictly require the condition  $\mu_{AO} + \mu_{BO_2} = \mu_{ABO_3} = E_{ABO_3}^{\text{bulk}}$ , and therefore  $\mu_{AO}$  and  $\mu_{BO_2}$  cannot vary independently. Further, if the system contains an excess of  $AO$ , the excess  $AO$  may form a bulk  $AO$  precipitate. Consequently, the chemical potential of  $AO$  may not exceed the chemical potential of bulk  $AO$ ;  $\mu_{AO} \leq E_{AO}^{\text{bulk}}$ . Similarly, the chemical potential of  $BO_2$  may not exceed that of bulk  $BO_2$ ;  $\mu_{BO_2} \leq E_{BO_2}^{\text{bulk}}$ . In other words, the following bounds on the chemical potentials have to be enforced:  $E_{ABO_3}^{\text{bulk}} - E_{BO_2}^{\text{bulk}} \leq \mu_{AO} \leq E_{AO}^{\text{bulk}}$  or equivalently  $E_{ABO_3}^{\text{bulk}} - E_{AO}^{\text{bulk}} \leq \mu_{BO_2} \leq E_{BO_2}^{\text{bulk}}$ .

Therefore, to compute the formation energy of the above reactions as a function of chemical potential, we conveniently define two extreme chemical potential limits; namely, the  $AO$ -rich and the  $AO$ -poor conditions. Specifically, for the  $AO$ -rich conditions we have

$$\mu_{AO} = E_{AO}^{\text{bulk}}, \quad (3a)$$

$$\mu_{BO_2} = E_{ABO_3}^{\text{bulk}} - E_{AO}^{\text{bulk}}. \quad (3b)$$

For the  $AO$ -poor conditions the two limiting chemical potentials are given by

$$\mu_{AO} = E_{ABO_3}^{\text{bulk}} - E_{BO_2}^{\text{bulk}}, \quad (3c)$$

$$\mu_{BO_2} = E_{BO_2}^{\text{bulk}}. \quad (3d)$$

Note that the  $AO$ -rich and the  $AO$ -poor limits map onto the  $BO_2$ -poor and the  $BO_2$ -rich limits, respectively, and beyond these limits, a bulk  $ABO_3$  perovskite phase will be thermodynamically unstable with respect to decomposition into its binary oxides. The chemical potential within these limits can be varied directly by changing of the concentrations of  $AO$  and  $BO_2$  or indirectly by control of the chemical potential of oxygen (oxidizing or reducing conditions). Finally, we note that under extreme reducing conditions, it may also be possible to reduce the binary metal oxides to their respective metallic phases and gaseous oxygen. In that case the chemical potential definitions need to be suitably modified to include also the energetics of the bulk metallic phases. However, in the present analysis we have ignored such extreme reducing conditions.

In Table II, we report the computed DFT (PBE) formation energies at the two extreme chemical-potential limits for the reactions given in Eqs. (2a)–(2d) for each of the six bulk single-perovskite chemistries considered here. Further, for each case we consider two different scenarios, where the Ce dopant and the associated charge-compensating defect (if applicable) are clustered at the nearest possible lattice sites or are isolated. For the former case, the dopant and the defect are modeled in the same supercell, whereas for the latter case, each defect is modeled in different supercells separately.

Figure 3 graphically presents the results reported in Table II. Red, yellow, green, and blue lines are used for  $Ce_A^{3+}$ ,  $Ce_A^{4+}$ ,  $Ce_B^{3+}$ , and  $Ce_B^{4+}$  doping situations, respectively. The solid lines represent the energetics for isolated-defect configurations, while the dashed lines are used for the clustered-defect configurations. The area between each pair of respective solid and dashed lines (depicting the energetics for the isolated and clustered defects) is filled, representing the expected variations in the computed defect energies due to the relative positions of the Ce

TABLE II. Ce-dopant formation energies as a function of Ce charge state and substitutional site according to the reactions given in Eqs. (2a)–(2d) and computed for the two extreme limits of the allowed chemical-potential ranges as per Eqs. (3a)–(3d) for the different *A*- and *B*-site chemistry. For each case, two different situations—where defects (i.e., Ce and the corresponding charge-compensating defect) are modeled in either a clustered or an isolated configuration—are considered. The most favorable defect formation energies at the two extreme chemical-potential limits are highlighted in bold for each  $ABO_3$  compound. See the text for details.

Perovskite	Equation	Ce doping	Defect formation energies			
			<i>AO</i> -poor conditions		<i>AO</i> -rich conditions	
			Isolated defects	Clustered defects	Isolated defects	Clustered defects
CaHfO <sub>3</sub>	(2a)	Ce <sub>Ca</sub> <sup>3+</sup>	<b>0.26</b>	0.40	0.92	1.06
ortho-	(2b)	Ce <sub>Hf</sub> <sup>3+</sup>	3.11	1.93	2.67	1.49
rhombohedral	(2c)	Ce <sub>Ca</sub> <sup>4+</sup>	1.17	1.47	2.05	2.35
<i>Pnma</i>	(2d)	Ce <sub>Hf</sub> <sup>4+</sup>	1.19	N/A	<b>0.76</b>	N/A
CaZrO <sub>3</sub>	(2a)	Ce <sub>Ca</sub> <sup>3+</sup>	<b>0.12</b>	0.40	0.60	0.88
ortho-	(2b)	Ce <sub>Zr</sub> <sup>3+</sup>	2.37	1.62	2.05	1.29
rhombohedral	(2c)	Ce <sub>Ca</sub> <sup>4+</sup>	0.90	1.36	1.56	2.01
<i>Pnma</i>	(2d)	Ce <sub>Zr</sub> <sup>4+</sup>	0.84	N/A	<b>0.52</b>	N/A
SrHfO <sub>3</sub>	(2a)	Ce <sub>Sr</sub> <sup>3+</sup>	<b>−0.23</b>	0.27	1.04	1.53
ortho-	(2b)	Ce <sub>Hf</sub> <sup>3+</sup>	2.63	1.81	1.79	0.97
rhombohedral	(2c)	Ce <sub>Sr</sub> <sup>4+</sup>	0.72	1.37	2.41	3.05
<i>Pnma</i>	(2d)	Ce <sub>Hf</sub> <sup>4+</sup>	0.92	N/A	<b>0.07</b>	N/A
SrZrO <sub>3</sub>	(2a)	Ce <sub>Sr</sub> <sup>3+</sup>	<b>−0.52</b>	0.21	0.56	1.30
ortho-	(2b)	Ce <sub>Zr</sub> <sup>3+</sup>	1.70	1.83	0.97	1.10
rhombohedral	(2c)	Ce <sub>Sr</sub> <sup>4+</sup>	0.23	1.14	1.68	2.60
<i>Pnma</i>	(2d)	Ce <sub>Zr</sub> <sup>4+</sup>	0.43	N/A	<b>−0.29</b>	N/A
BaHfO <sub>3</sub>	(2a)	Ce <sub>Ba</sub> <sup>3+</sup>	<b>0.67</b>	0.93	2.51	2.77
cubic	(2b)	Ce <sub>Hf</sub> <sup>3+</sup>	2.81	1.84	1.58	0.62
<i>Pm</i> $\bar{3}m$	(2c)	Ce <sub>Ba</sub> <sup>4+</sup>	2.40	2.23	4.85	4.68
	(2d)	Ce <sub>Hf</sub> <sup>4+</sup>	1.12	N/A	<b>−0.10</b>	N/A
BaZrO <sub>3</sub>	(2a)	Ce <sub>Ba</sub> <sup>3+</sup>	<b>0.64</b>	1.01	2.33	2.70
cubic	(2b)	Ce <sub>Zr</sub> <sup>3+</sup>	1.91	1.53	0.79	0.41
<i>Pm</i> $\bar{3}m$	(2c)	Ce <sub>Ba</sub> <sup>4+</sup>	2.31	2.08	4.56	4.33
	(2d)	Ce <sub>Zr</sub> <sup>4+</sup>	0.73	N/A	<b>−0.39</b>	N/A

N/A, not applicable.

dopants and the associated charge-compensating defects. It can be seen from Fig. 3 that irrespective of the chemistry, the defect configurations with either Ce<sup>3+</sup> at the *A* site or Ce<sup>4+</sup> at the *B* site [depicted by red and blue lines and given by Eqs. (2a) and (2d), respectively] consistently result in the lowest defect formation energies. On the other hand, doping situations with Ce<sup>3+</sup> at the *B* site and Ce<sup>4+</sup> at the *A* site always result in higher energies, irrespective of the chemical potential. While the trends exhibited by zirconates and hafnates are qualitatively very similar, changing the *A*-site chemistry from Ca to Sr to Ba results in a systematic variation in the defect energetics. For instance, the range of chemical potential for which Ce<sub>*A*</sub><sup>3+</sup> (Ce<sub>*B*</sub><sup>4+</sup>) is predicted to be thermodynamically stable gradually decreases (increases) on going from Ca to Ba in both the zirconate and the hafnate compounds.

### C. Electronic structure of Ce<sub>*A*</sub><sup>3+</sup> and Ce<sub>*B*</sub><sup>4+</sup> dopants

From the results presented in the previous section, it is clear that depending on the chemical potential (or synthesis

conditions), Ce<sup>3+</sup> doping at the *A* site [Eq. (2a)] and Ce<sup>4+</sup> doping at the *B* site [Eq. (2d)] are the thermodynamically most favored cases for solution of Ce in  $ABO_3$  perovskites. In this section, we compare qualitative details of the electronic structure between Ce<sup>3+</sup> doping at the *A* site and Ce<sup>4+</sup> doping at the *B* site, with the aim to understand and contrast their scintillation behavior in an  $ABO_3$  host environment.

From an electronic-structure point of view, a necessary condition for scintillation in Ce-doped materials is that the Ce 4*f* and 5*d* levels must both lie within the host band gap and should also have suitable positions with respect to host valence- and conduction-band edges, respectively. The first is an absolutely necessary criterion for scintillation, while the second is critical for performance. If the Ce 4*f* (5*d*) level is buried in the valence (conduction) band of the host, then there will be no Ce-activated scintillation. On the other hand, a Ce 4*f* level that lies too high above the VBM is also not desirable, as it leads to a poor hole-capture probability at the activator site. Furthermore, if the Ce<sup>3+</sup>

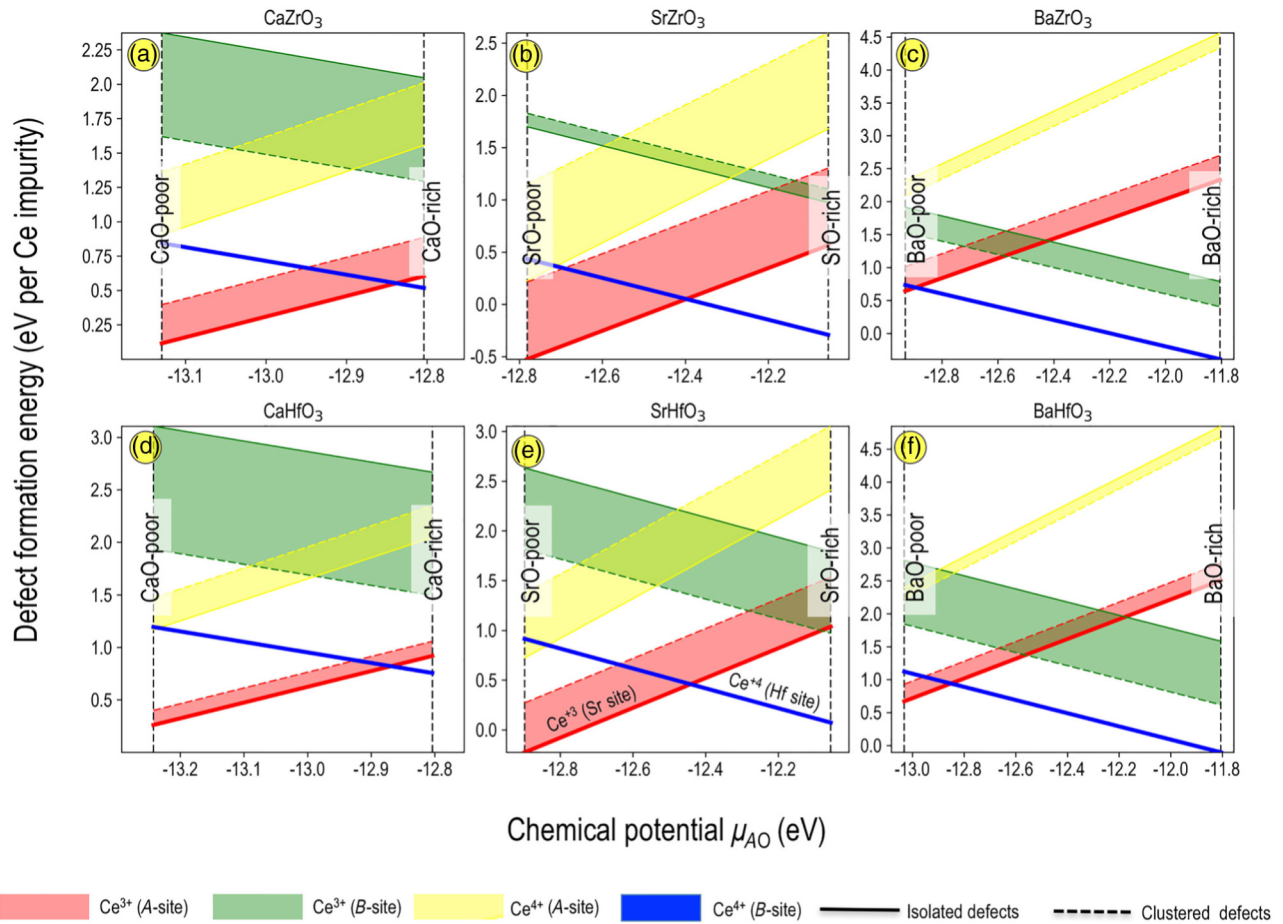


FIG. 3. Chemical-potential-dependent Ce-dopant formation energies computed as a function of the Ce charge state (i.e., 3+ or 4+) and the substitutional sites (i.e., the  $A$ - or  $B$ -cation site) in the respective ground-state structures of the  $ABO_3$  perovskites. In each case, the energy range covered by different possible configurations of the defect clusters is highlighted with different color fills and the solid and dashed lines represent the two extreme cases where the defect clusters are modeled in isolated or closely clustered configurations, respectively. The two extreme (i.e., the  $AO$ -poor and  $AO$ -rich) chemical-potential limits are given as per the reactions in Eqs. (3a)–(3d).

excited state  $(Ce^{3+})^*$  lies below but too close to the CBM, then thermal excitations from the  $5d$  state into the conduction band can, in principle, reduce or even completely quench luminescence, thereby leading to a poor scintillator. Finally, too large an energy difference in the CBM and the excited-state level would also decrease the probability for the Ce ion to capture an electron since more phonon modes would need to be available to dissipate the large energy.

As a natural next step, we employ DFT computations to calculate the relative positions and associated charge densities of the Ce  $4f$  and  $5d$  states with respect to host valence- and conduction-band edges, respectively. Ce dopants with 3+ (for the  $A$  site) and 4+ (for the  $B$  site) charge states are modeled in a sufficiently large supercell (i.e., a supercell that allows us to recover a bulk-like behavior away from the dopant) by our periodically repeating the unit cell of the host crystal. We allow for relaxation of all the internal coordinates while keeping the cell dimensions

fixed to those of the bulk. While for the  $B$ -site doping, Ce naturally adopts a 4+ charge state and thus preserves the charge of the original  $B$  ion, one electron per Ce atom is removed from the supercell for the  $A$ -site doping situations and a neutralizing background charge is used for simulation of the charged supercells and to describe the 3+ charge state. We also note that the aim in these studies is to model an isolated Ce dopant in an infinite host crystal; however, in practice the finite-supercell approach may introduce spurious dopant-dopant interactions due to the periodic boundary conditions, which in turn result in a broadening of the impurity levels into bands. Although filled and empty  $4f$  levels—for  $Ce^{3+}$  and  $Ce^{4+}$  dopants, respectively—are typically atom-like and therefore highly localized, the bands associated with Ce-localized  $5d$  states typically exhibit some dispersion due to finite-size effects as well as some degree of hybridization with the host  $d$  states forming the CBM. Despite these complications, the electronic-structure analysis based on DFT computations

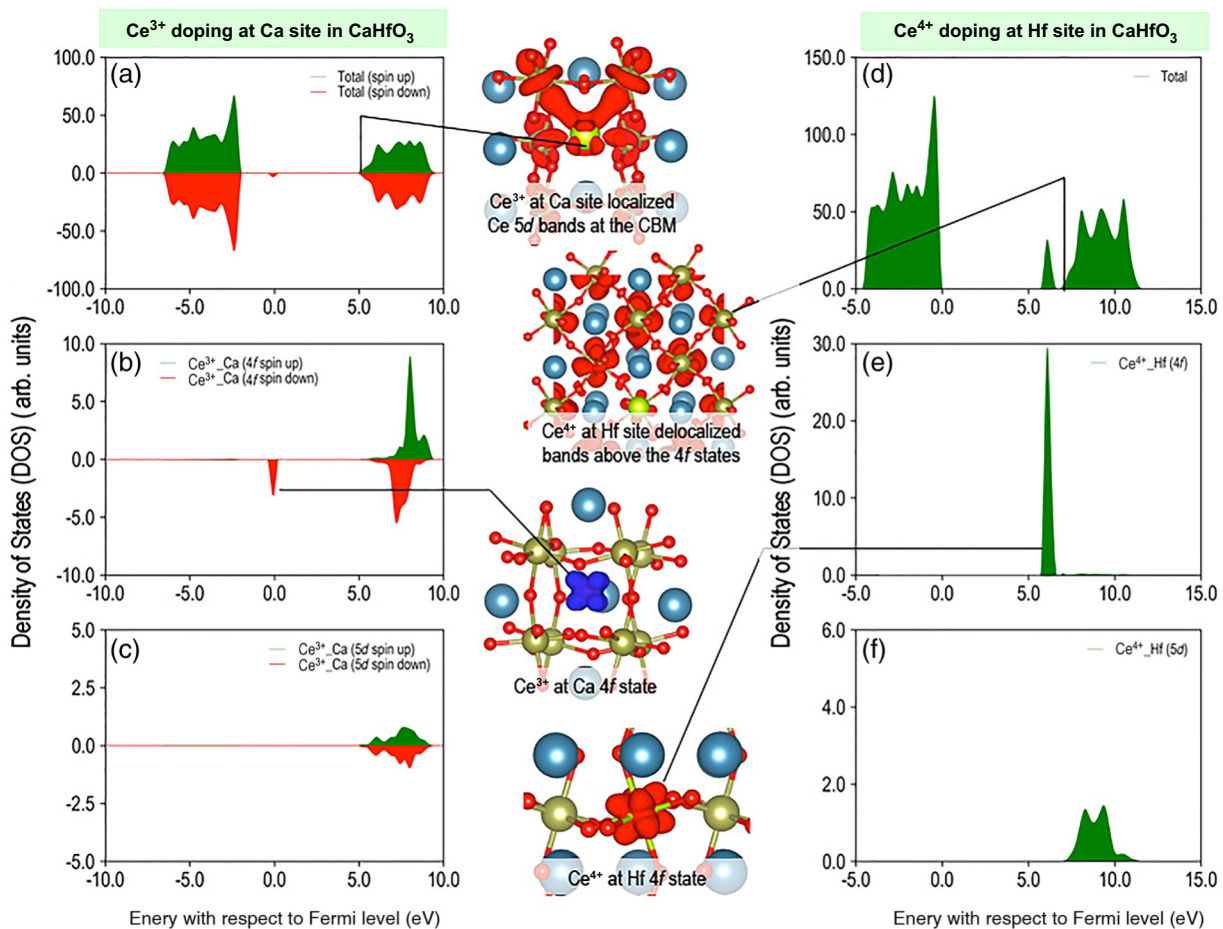


FIG. 4. Total and partial (Ce  $4f$  and  $5d$ ) density of states for the two most stable (depending on the chemical potential) Ce substitutional doping configurations in  $\text{CaHfO}_3$  computed with the HSE hybrid functional with  $\alpha = 0.4$ . (a) Total, (b) Ce  $4f$ , and (c) Ce  $5d$  states for a  $\text{Ce}^{3+}$  dopant at the Ca site. (d)–(f) The corresponding results for a  $\text{Ce}^{4+}$  dopant at the Hf site. For the  $\text{Ce}^{3+}$  dopant, spin-up and spin-down states are colored green and red, respectively. In each panel, the zero of energy corresponds to the Fermi level. The central panels show the band-decomposed charge density corresponding to the conduction-band edges (the top two configurations) and the Ce-dopant  $4f$  states (the bottom two configurations) for supercells containing a  $\text{Ce}^{3+}$  dopant at the Ca site and a  $\text{Ce}^{4+}$  dopant at the Hf site, respectively.

can be practically useful in understanding the relative trends across chemistries, albeit in a qualitative manner.

To compare and contrast key differences in the electronic structure of the  $\text{Ce}_A^{3+}$  and  $\text{Ce}_B^{4+}$  dopants, Fig. 4 presents our results for the total and partial density of states and band-decomposed charge-density analyses for  $\text{CaHfO}_3$  computed with hybrid DFT (i.e., the HSE functional with  $\alpha = 0.4$ , as discussed in Sec. III A). Note that the presentation of  $\text{CaHfO}_3$  is for illustration only; qualitatively similar results are obtained for the other  $\text{ABO}_3$  compounds, as presented in the Supplemental Material [105].

Figures 4(a)–4(c) present the total and site-projected partial density of states (for Ce  $4f$  and  $5d$  states) for  $\text{Ce}^{3+}$  doping at the Ca site. The Ce  $4f$  state localizes within the band gap approximately 2.0 eV above the VBM and is singly occupied. This is further confirmed by our plotting

the total spin charge density for the supercell (which also exactly matches with the Ce  $4f$  band-decomposed charge density) shown in Fig. 4. As briefly discussed above, unlike the Ce  $4f$  state, the  $5d$  states are relatively more dispersed, owing to their hybridization with the Hf  $5d$  states, and form the bottom of the conduction-band edge. A plot of the band-decomposed charge density for the band associated with the CBM clearly shows that the density is largely localized on the Ce atom and the surrounding Hf atoms, alluding to a high probability of localization of an excited electron to the activator site on relaxation to the conduction-band edge.

While looking at the charge density associated with empty bands forming the conduction-band edge is insightful, it is worthwhile to note that a ground-state calculation with the  $4f$  level filled and the  $5d$  level empty generally gives rise to a  $5d$  level that will be higher in energy than

when the  $5d$  level is filled and the  $4f$  level is empty. This effect can be simply understood on the basis of screening arguments. Since the  $4f$  level is closer to the nucleus than the  $5d$  level, a filled  $4f$  level can effectively screen the  $5d$  level from an attractive Coulombic interaction with the nucleus. However, when the  $4f$  level is emptied, the screening effect from the positive nuclei will be reduced and the  $5d$  level will relax to a lower energy. Therefore, from a mechanistic point of view it is more relevant to simulate an excited  $5d$  level in  $\text{Ce}^{3+}$  (i.e., when the unpaired electron is transferred from the  $4f$  level to the lowest  $5d$  level of the dopant), also frequently denoted as  $(\text{Ce}^{3+})^*$ . However, an accurate determination of the Ce  $5d$  level below the CBM in the  $(\text{Ce}^{3+})^*$  excited state, in principle, requires many-body approaches beyond conventional DFT, which can be extremely challenging and computationally demanding for large supercells. Alternatively, we perform excited-state (constrained-hybrid-DFT) calculations to verify that the Ce  $5d$  level does indeed lower by about 0.6 eV with respect to the VBM in the  $(\text{Ce}^{3+})^*$  excited state. Finally, we note that the Stokes shift can also be computed by allowing for lattice relaxation around the  $(\text{Ce}^{3+})^*$  state, which further lowers the  $5d$  level. However, studies have pointed out that the Stokes shift is difficult to model accurately with DFT-based band-structure calculations. Since here we aim toward a comparative qualitative understanding of the electronic structure of Ce as a function of the charge state and substitutional site, we do not try to model the Stokes shift explicitly in our simulations, and the excited state is simulated without our allowing for the geometric relaxation.

While the  $\text{Ce}^{3+}$  dopant at the Ca site provides a favorable band structure in terms of the VBM- $4f$  gap as well as a suitably localized  $5d$  state near the CBM, details of the electronic structure for a  $\text{Ce}^{4+}$  dopant at the Hf site—shown in Figs. 4(d)–4(f)—present a sharp contrast. Most prominently, the empty  $4f$  level in  $\text{Ce}^{4+}$ , still localized at the activator site, shifts toward higher energy, widening the VBM- $4f$  charge-transfer gap considerably. Furthermore, the  $5d$  states in  $\text{Ce}^{4+}$  at the Hf site are predicted to be deeper, buried inside the conduction band. The CBM in this case is formed largely by the Hf  $5d$  states, which are fairly delocalized, as can be seen from the band-decomposed charge density associated with the conduction-band edge plotted in Fig. 4. Therefore, unlike the  $\text{Ce}^{3+}$  dopant at the Ca site, in this case the  $4f$  and  $5d$  levels of the Ce activator are both unfavorably located in the band gap, as a result of which  $\text{Ce}^{4+}$  dopant at the Hf site is highly unlikely to exhibit a scintillating behavior. From our analysis, this charge-state dependence of the  $4f$  and  $5d$  levels for a Ce impurity—schematically depicted in Fig. 5—is not specific to  $\text{CaHfO}_3$  and is anticipated to be valid, in general, for any  $A^{2+}B^{4+}O_3$ -type perovskite chemistry. We note that qualitatively similar charge-state-dependent shifts in the Ce levels have recently

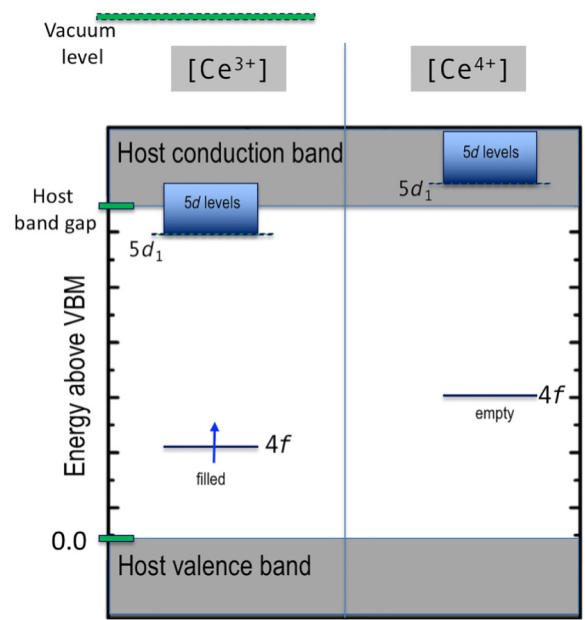


FIG. 5. Charge-state dependence (i.e.,  $3+$  versus  $4+$ ) of the  $4f$  and  $5d$  levels for a Ce impurity in an  $ABO_3$  host environment. Note that the comparison in the illustration is meant only for a qualitative understanding.

been reported both theoretically and experimentally in garnets [30].

#### IV. DISCUSSION AND CONCLUSIONS

While our theoretical investigation relies on a number of approximations/simplifications, as discussed in the previous section, to make the computational method adopted efficient, practical, and tractable, it already provides useful insights into previously reported experimental observations. Most notably, our work demonstrates that the observed scintillating behavior of  $ABO_3$  compounds can be directly attributed to the  $\text{Ce}^{3+}$  charge state, and the  $\text{Ce}^{4+}$  state is incapable of acting as a luminescent center. This is in remarkable agreement with the fact that the experimental investigations that reported radioluminescence in  $ABO_3$ -perovskite-based phosphors and scintillators mainly relied on strategies that tend to stabilize the  $\text{Ce}^{3+}$  charge state relative to the  $\text{Ce}^{4+}$  state. For instance, co-doping with various charge-compensating metal ions such as Lu, Al, and Ta ions [22] or Li ions [23] that leads to radioluminescence is naturally expected to favor the  $3+$  charge state for Ce. Furthermore, as evident from our chemical-potential-dependent defect-formation-energy analysis, heavy  $A$ -site doping of Ce in a highly- $A$ -deficient perovskite (i.e.,  $AO$  poor) that results in good luminescence performance would also favor the  $\text{Ce}^{3+}$  charge state at the  $A$  site [24]. Finally, the luminescence reported as a result of synthesis of compounds in highly

reducing conditions [25] can also be understood by noting that the *AO*-poor condition allows a lower bound on the possible range of oxygen chemical potential and therefore favors a more reducing environment as compared with the *AO*-rich condition. More precisely, the bounds on the oxygen chemical potential can be written as  $\mu_{AO} - \mu_A \leq \mu_O \leq 1/2\mu_{O_2}^{\text{gas}}$ . Since  $\mu_{AO}$  is always lower in *AO*-poor conditions than in *AO*-rich conditions, this translates to a lower allowed bound for  $\mu_O$ , therefore allowing for a more reducing condition. Our results for the Ce substitutional defect formation energies also correlate well with previously reported experimental observations. For instance, Loureiro *et al.* [22] observed that a SrHfO<sub>3</sub> host lattice with higher relative percentages of Ce<sup>3+</sup> can be obtained under much milder conditions as compared with BaHfO<sub>3</sub>. In close agreement with the experimental results, a comparison between the computed defect formation energies of SrHfO<sub>3</sub> and BaHfO<sub>3</sub> clearly shows lower formation energies and a wider stability range for Ce<sup>3+</sup> at the Sr site in SrHfO<sub>3</sub> as compared with Ce<sup>3+</sup> at the Ba site in BaHfO<sub>3</sub>. Lastly, we note that the energy-level diagrams of Ce<sup>3+</sup> and Ce<sup>4+</sup> in Gd<sub>3</sub>Ga<sub>3</sub>Al<sub>2</sub>O<sub>12</sub> garnet were recently established experimentally and indicate a higher position of the 5*d*<sup>1</sup> state of Ce<sup>4+</sup> in the forbidden gap in comparison with that of Ce<sup>3+</sup>, again in qualitative agreement with the results obtained in our electronic-structure analysis [30].

In summary, we used first-principles conventional-DFT and hybrid-functional computations to study (i) the relative trends in the structure, energetics, and electronic structure of bulk *ABO*<sub>3</sub> perovskites, (ii) the relative energetics of preferential solution sites for Ce as a function of the charge state, chemical potential, and defect configurations in Ce-doped perovskites, and (iii) the electronic structure of the most stable Ce-doping configurations (given by a combination of the preferred substitutional site and energetically favored charge state) identified as a function of the prevalent chemical potential by looking at the total density of states and the dopant's partial density of states and band-decomposed charge-density analysis. Our computational results for the bulk perovskites compare favorably with previously reported experimental results and reconfirm well-understood systematic chemical trends in structure, energetics, and electronic structure across the targeted chemistries. Subsequently, our analysis for chemical-potential-dependent Ce substitutional dopant formation energies reveals that a Ce<sup>3+</sup> substitutional dopant is always favored at the *A* site in a reducing environment, whereas a Ce<sup>4+</sup> substitutional defect is consistently favored at the *B* site in an oxidizing environment. Further electronic-structure analysis shows that while depending on the experimental synthetic conditions both Ce<sup>3+</sup> at the *A* site and Ce<sup>4+</sup> at the *B* site can, in principle, be thermodynamically stable, only Ce<sup>3+</sup> at the *A* site exhibits a favorable electronic structure that can potentially support the experimentally observed scintillating behavior

and the Ce<sup>4+</sup> charge state is unlikely to manifest any luminescence. Our results, although expected to be qualitative, are discussed in relation to previously reported experimental findings and display excellent agreement with available experimental observations. In general, it is demonstrated that controlling the charge state and substitutional sites of Ce could be yet another way (in addition to band-gap and band-edge engineering) to manipulate the relative position of scintillating states with respect to valence- and conduction-band edges.

## ACKNOWLEDGMENTS

G.P., B.P.U., and C.R.S. gratefully acknowledge support from the Laboratory Directed Research and Development program within Los Alamos National Laboratory (LANL)—an affirmative-action equal-opportunity employer operated by Los Alamos National Security LLC for the National Nuclear Security Administration of the U.S. Department of Energy under Contract No. DEAC52-06NA25396. Computational support for this work was provided by LANL's high-performance-computing clusters.

- 
- [1] G. F. Knoll, *Radiation Detection, and Measurement* (Wiley, New York, 2010).
  - [2] G. Blasse, Scintillation materials, *Chem. Mater.* **6**, 1465 (1994).
  - [3] P. A. Rodnyi, *Physical Processes in Inorganic Scintillators* (CRC Press, Boca Raton, 1997).
  - [4] M. J. Weber, Inorganic scintillators: Today and tomorrow, *J. Lumin.* **100**, 35 (2002).
  - [5] M. Nikl and A. Yoshikawa, Recent R&D trends in inorganic single-crystal scintillator materials for radiation detection, *Adv. Opt. Mater.* **3**, 463 (2015).
  - [6] Paul Lecoq, Alexander Gektin, and Mikhail Korzhik, *Inorganic Scintillators for Detector Systems: Physical Principles and Crystal Engineering* (Springer, New York, 2016).
  - [7] P. A. Rodnyi, P. Dorenbos, and C. W. E. van Eijk, Energy loss in inorganic scintillators, *Phys. Stat. Sol. (b)* **187**, 15 (1995).
  - [8] M. Nikl, Scintillation detectors for x-rays, *Meas. Sci. Technol.* **17**, R37 (2006).
  - [9] R. Hofstadter, The detection of gamma-rays with thallium-activated sodium iodide crystals, *Phys. Rev.* **75**, 796 (1949).
  - [10] W. van Sciver and R. Hofstadter, Scintillations in thallium-activated CaI<sub>2</sub> and CsI, *Phys. Rev.* **84**, 1062 (1951).
  - [11] K. W. Krämer, P. Dorenbos, H. U. Güdel, and C. W. E. Van Eijk, Development and characterization of highly efficient new cerium doped rare earth halide scintillator materials, *J. Mater. Chem.* **16**, 2773 (2006).
  - [12] M. Nikl, A. Yoshikawa, K. Kamada, K. Nejezchleb, C. R. Stanek, J. A. Mares, and K. Blazek, Development of

- LuAG-based scintillator crystals: A review, *Prog. Cryst. Growth Charact. Mater.* **59**, 47 (2013).
- [13] M. Nikl, A. Vedda, and V. V. Laguta, in *Springer Handbook of Crystal Growth*, edited by G. Dhanaraj, K. Byrappa, V. Prasad, and M. Dudley (Springer, Heidelberg, 2010), p. 1663.
- [14] V. Jary, M. Nikl, S. Kurosawa, Y. Shoji, E. Mihokova, A. Beitlerova, G. P. Pazzi, and A. Yoshikawa, Luminescence characteristics of the Ce<sup>3+</sup>-doped pyrosilicates: The case of La-admixed Gd<sub>2</sub>Si<sub>2</sub>O<sub>7</sub> single crystals, *J. Phys. Chem. C* **118**, 26521 (2014).
- [15] M. D. Birowsuto, D. Cortecchia, W. Drozdowski, K. Brylew, W. Lachmanski, A. Bruno, and C. Socib, X-ray scintillation in lead halide perovskite crystals, *Sci Rep.* **6**, 37254 (2016).
- [16] T. Yanagida, Study of rare-earth-doped scintillators, *Opt. Mater.* **35**, 1987 (2013).
- [17] L. Casillas-Trujillo, D. A. Andersson, B. Dorado, M. Nikl, K. E. Sickafus, K. J. McClellan, and C. R. Stanek, Intrinsic defects, nonstoichiometry, and aliovalent doping of A<sup>2+</sup>B<sup>4+</sup>O<sub>3</sub> perovskite scintillators, *Phys. Status Solidi B* **251**, 2279 (2014).
- [18] E. V. van Loef, W. M. Higgins, J. Glodo, A. Lempicki, V. Venkataramani, W. W. Moses, S. E. Derenzo, and K. S. Shah, Scintillation properties of SrHfO<sub>3</sub>:Ce<sup>3+</sup> and BaHfO<sub>3</sub>:Ce<sup>3+</sup> ceramics, *IEEE Trans. Nucl. Sci.* **54**, 741 (2007).
- [19] C. Michail, N. Kalyvas, I. Valais, S. David, I. Seferis, A. Toutountzis, A. Karabotsos, P. Liaparinis, G. Fountos, and I. Kandarakis, On the response of GdAlO<sub>3</sub>:Ce powder scintillators, *J. Lumin.* **144**, 45 (2013).
- [20] W. Drozdowski, A. J. Wojtowicz, T. Lukasiewicz, and J. Kisielewski, Scintillation properties of LuAP and LuYAP crystals activated with Cerium and Molybdenum, *Nucl. Instr. Meth. Phys. Res. A* **562**, 254 (2006).
- [21] A. J. Wojtowicz, J. Glodo, W. Drozdowski, and K. R. Przegietka, Electron traps and scintillation mechanism in YAlO<sub>3</sub>: Ce and LuAlO<sub>3</sub>: Ce scintillators, *J. Lumin.* **79**, 275 (1998).
- [22] Sergio M. Loureiro, Yan Gao, and Venkat Venkataramani, Stability of Ce(III) activator and codopant effect in MHfO<sub>3</sub> (M = Ba, Sr) scintillators by XANES, *J. Am. Ceram. Soc.* **88**, 219(2005).
- [23] Y. M. Ji, D. Y. Jiang, L. S. Qin, J. J. Chen, T. Feng, Y. K. Liao, Y. P. Xu, and J. L. Shi, Preparation and luminescent properties of nanocrystals of Ce<sup>3+</sup>-activated SrHfO<sub>3</sub>, *J. Cryst. Growth* **280**, 93 (2005).
- [24] M. Nikl, P. Bohacek, B. Trunda, V. Jary, V. Studnicka, R. Kucerkova, and A. Beitlerova, SrHfO<sub>3</sub>-based phosphors and scintillators, *Opt. Mater.* **34**, 433 (2011).
- [25] A. Grezer, E. Zych, and L. Kepinski, BaHfO<sub>3</sub>: Ce sintered ceramic scintillators, *Radiat. Meas.* **45**, 386 (2010).
- [26] J. Andriessen, E. van der Kolk, and P. Dorenbos, Lattice relaxation study of the 4f-5d excitation of Ce<sup>3+</sup>-doped LaCl<sub>3</sub>, LaBr<sub>3</sub>, and NaLaF<sub>4</sub>: Stokes shift by pseudo Jahn-Teller effect, *Phys. Rev. B* **76**, 075124 (2007).
- [27] C. Ortiz, O. Eriksson, and M. Klintonberg, Data mining and accelerated electronic structure theory as a tool in the search for new functional materials, *Comp. Mater. Sci.* **44**, 1042 (2009).
- [28] W. Setyawan, R. M. Gaume, S. Lam, R. S. Feigelson, and S. Curtarolo, High-throughput combinatorial database of electronic band structures for inorganic scintillator materials, *ACS Combinatorial Sci.* **13**, 382 (2011).
- [29] M. Fasoli, A. Vedda, M. Nikl, C. Jiang, B. P. Uberuaga, D. A. Andersson, K. J. McClellan, and C. R. Stanek, Band-gap engineering for removing shallow traps in rare-earth Lu<sub>3</sub>Al<sub>5</sub>O<sub>12</sub> garnet scintillators using Ga<sup>3+</sup> doping, *Phys. Rev. B* **84**, 081102(R) (2011).
- [30] Y. Wu, F. Meng, Q. Li, M. Koschan, and C. L. Melcher, Role of Ce<sup>4+</sup> in the Scintillation Mechanism of Codoped Gd<sub>3</sub>Ga<sub>3</sub>Al<sub>2</sub>O<sub>12</sub>:Ce, *Phys. Rev. Applied* **2**, 044009 (2014).
- [31] S. K. Yadav, B. P. Uberuaga, M. Nikl, C. Jiang, and C. R. Stanek, Band-Gap and Band-Edge Engineering of Multicomponent Garnet Scintillators from First Principles, *Phys. Rev. Applied* **4**, 054012 (2015).
- [32] A. Canning, A. Chaudhry, R. Boutchko, and N. Grønbech-Jensen, First-principles study of luminescence in Ce-doped inorganic scintillators, *Phys. Rev. B* **83**, 125115 (2011).
- [33] K. Biswas and M.-H. Du, Energy transport and scintillation of cerium-doped elpasolite Cs<sub>2</sub>LiYCl<sub>6</sub>: Hybrid density functional calculations, *Phys. Rev. B* **86**, 014102 (2012).
- [34] A. Chaudhry, R. Boutchko, S. Chourou, G. Zhang, N. Grønbech-Jensen, and A. Canning, First-principles study of luminescence in Eu<sub>2+</sub>-doped inorganic scintillators, *Phys. Rev. B* **89**, 155105 (2014).
- [35] L. Petit, A. Svane, Z. Szotek, and W. M. Temmerman, First-principles study of rare-earth oxides, *Phys. Rev. B* **72**, 205118 (2005).
- [36] M. Stephan, M. Zachau, M. Groting, O. Karplak, V. Eyert, K. Mishra, and P. Schmidt, A theoretical investigation of 4f-5d transition of trivalent rare earth ions in fluorides and complex oxides, *J. Lumin.* **114**, 255 (2005).
- [37] Y. Wu, Q. Li, S. Jones, C. Dun, S. Hu, M. Zhuravleva, A. C. Lindsey, L. Stand, M. Loyd, M. Koschan, J. Auxier II, H. L. Hall, and C. L. Melcher, Defect Engineering by Codoping in KCaI<sub>3</sub>:Eu<sup>2+</sup> Single-Crystalline Scintillators, *Phys. Rev. Applied* **8**, 034011 (2017).
- [38] A. I. Liechtenstein, V. I. Anisimov, and J. Zaane, First-principles calculations of the electronic structure and spectra of strongly correlated systems: The LDA+ U method, *Phys. Rev. B* **52**, R5467 (1995).
- [39] S. L. Dudarev, G. A. Botton, S. Y. Savrasov, C. J. Humphreys, and A. P. Sutton, Electron-energy-loss spectra and the structural stability of nickel oxide: An LSDA+U study, *Phys. Rev. B* **57**, 1505 (1998).
- [40] S. Watanabe and K. Ogasawara, Experimental and first-principles analysis of 4f-5d absorption spectrum for Ce<sub>3+</sub> in LiYF<sub>4</sub> considering lattice relaxation, *J. Phys. Soc. Jpn.* **77**, 084702 (2008).
- [41] J. Heyd, G. E. Scuseria, and M. Ernzerhof, Hybrid functionals based on a screened Coulomb potential, *J. Chem. Phys.* **118**, 8207 (2003).
- [42] J. P. Perdew, M. Ernzerhof, and K. Burke, Rationale for mixing exact exchange with density functional approximations, *J. Chem. Phys.* **105**, 9982 (1996).

- [43] J. P. Perdew, K. Burke, and M. Ernzerhof, Generalized Gradient Approximation Made Simple, *Phys. Rev. Lett.* **77**, 3865 (1996).
- [44] A. V. Krugau, O. A. Vydrov, A. F. Izmaylov, and G. E. Scuseria, Influence of the exchange screening parameter on the performance of screened hybrid functionals, *J. Chem. Phys.* **125**, 224106 (2006).
- [45] G. Kresse and J. Furthmüller, Efficient iterative schemes for ab initio total-energy calculations using a plane-wave basis set, *Phys. Rev. B* **54**, 11169 (1996).
- [46] G. Kresse and D. Joubert, From ultrasoft pseudopotentials to the projector augmented-wave method, *Phys. Rev. B* **59**, 1758 (1999).
- [47] P. E. Blöchl, Projector augmented-wave method, *Phys. Rev. B* **50**, 17953 (1994).
- [48] H. J. Monkhorst and J. D. Pack, Special points for Brillouin-zone integrations, *Phys. Rev. B* **13**, 5188 (1976).
- [49] G. Makov and M. C. Payne, Periodic boundary conditions in ab initio calculations, *Phys. Rev. B* **51**, 4014 (1995).
- [50] J. Paier, M. Marsman, K. Hummer, G. Kresse, I. C. Gerber, and J. G. Angyan, Screened hybrid density functionals applied to solids, *J. Chem. Phys.* **124**, 154709 (2006).
- [51] C. C. Wang, G. Pilania, and R. Ramprasad, Dielectric properties of carbon-, silicon-, and germanium-based polymers: A first-principles study, *Phys. Rev. B* **87**, 035103 (2013).
- [52] A. Mannodi-Kanakkithodi, G. Pilania, T. D. Huan, T. Lookman, and R. Ramprasad, Machine learning strategy for accelerated design of polymer dielectrics, *Sci. Rep.* **6**, 20952 (2016).
- [53] H.-P. Komsa, P. Broqvist, and A. Pasquarello, Alignment of defect levels and band edges through hybrid functionals: Effect of screening in the exchange term, *Phys. Rev. B* **81**, 205118 (2010).
- [54] P. Broqvist, A. Alkauskas, and A. Pasquarello, Defect levels of dangling bonds in silicon and germanium through hybrid functionals, *Phys. Rev. B* **78**, 075203 (2008).
- [55] A. Alkauskas, P. Broqvist, F. Devynck, and A. Pasquarello, Band Offsets at Semiconductor-oxide Interfaces from Hybrid Density-functional Calculations, *Phys. Rev. Lett.* **101**, 106802 (2008).
- [56] H. D. Megaw, Crystal structure of double oxides of the perovskite type, *Proc. Phys. Soc.* **58**, 133 (1946).
- [57] I. Levin, T. G. Amos, S. M. Bell, L. Farber, T. A. Vanderah, R. S. Roth, and B. H. Toby, Phase equilibria, crystal structures, and dielectric anomaly in the BaZrO<sub>3</sub>-CaZrO<sub>3</sub> system, *J. Solid State Chem.* **175**, 170 (2003).
- [58] A. M. Glazer, The classification of tilted octahedra in perovskites, *Acta Cryst. B* **28**, 3384 (1972).
- [59] V. M. Goldschmidt, Die gesetze der krystallochemie, *Naturwissenschaften* **21**, 477 (1926).
- [60] A. Feteira, D. C. Sinclair, K. Z. Rajab, and M. T. Lanagan, Crystal structure and microwave dielectric properties of alkaline earth hafnates, AHfO<sub>3</sub> (A = Ba, Sr, Ca), *J. Am. Ceram. Soc.* **91**, 893 (2008).
- [61] I. M. Reaney, E. L. Colla, and N. Setter, Dielectric and structural characteristics of Ba-based and Sr-based complex perovskites as a function of tolerance factor, *Jpn. J. Appl. Phys.* **1**, 3984 (1994).
- [62] H. J. A. Koopmans, G. M. H. van de Velde, and P. J. Gellings, Powder neutron diffraction study of the perovskites CaTiO<sub>3</sub> and CaZrO<sub>3</sub>, *Acta Cryst.* **C39**, 1323 (1983).
- [63] Y. Zhao and D. J. Weidner, Thermal expansion of SrZrO<sub>3</sub> and BaZrO<sub>3</sub> perovskites, *Phys. Chem. Minerals* **18**, 294 (1991).
- [64] I. Charrier-Cougoulic, T. Pagnier, and G. Lucazeau, Raman spectroscopy of perovskite-type BaCe<sub>x</sub>Zr<sub>1-x</sub>O<sub>3</sub> (0 ≤ x ≤ 1), *J. Solid State Chem.* **142**, 220 (1999).
- [65] P. Dorenbos, The electronic structure of lanthanide doped compounds with 3d, 4d, 5d, or 6d conduction band states, *J. Lumin.* **151**, 224 (2014).
- [66] J. J. Robertson, Band offsets of wide-band-gap oxides and implications for future electronic devices, *Vac. Sci. Technol. B* **18**, 1785 (2000).
- [67] D. J. Lee, Y. K. Seo, Y. S. Lee, and H.-J. Noh, Spectroscopic investigation on the electronic structure of a 5d band insulator SrHfO<sub>3</sub> in proximity to ferroelectric instability: Comparison with SrTiO<sub>3</sub> and SrZrO<sub>3</sub>, *Solid State Commun.* **150**, 301 (2010).
- [68] C. Azahaf, H. Zaari, A. Abbassi, H. Ez-Zahraouy, and A. Benyoussef, Theoretical investigation of spontaneous polarization, electronic and optical properties of cubic perovskite BaHfO<sub>3</sub>, *Opt. Quant. Electron.* **47**, 2889 (2015).
- [69] R. Ganguly, V. Siruguri, I. K. Gopalakrishnan, and J. V. Yakhmi, Stability of the layered Sr<sub>3</sub>Ti<sub>2</sub>O<sub>7</sub> structure in La<sub>1.2</sub>(Sr<sub>1-x</sub>Ca<sub>x</sub>)<sub>1.8</sub>Mn<sub>2</sub>O<sub>7</sub>, *J. Phys.: Condens. Matter* **12**, 1683 (2000).
- [70] D. Taylor, Thermal expansion data. I: Binary oxides with the sodium chloride and wurtzite structures, MO., *Trans. Brit. Ceram. Soc.* **83**, 5 (1984).
- [71] L.-G. Lieu and W. A. Bassett, Effect of pressure on the crystal structure and the lattice parameters of BaO, *J. Geophys. Res.* **77**, 4934 (1972).
- [72] C. J. Howard, R. J. Hill, and B. E. Reichert, Structures of ZrO<sub>2</sub> polymorphs at room temperature by high-resolution neutron powder diffraction, *Acta Crystallogr. B* **44**, 116 (1988).
- [73] R. E. Hann, P. R. Suitch, and J. L. Pentecost, Monoclinic crystal structures of ZrO<sub>2</sub> and HfO<sub>2</sub> refined from x-ray powder diffraction data, *J. Am. Ceram. Soc.* **68**, 285 (1985).
- [74] S. Stølen, in *Experimental Thermodynamics, Volume VI: Measurement of the Thermodynamics Properties of Single Phases*, edited by A. R. H. Goodwin, K. N. Marsh, and W. A. Wakeham (Elsevier, Amsterdam, 2003), p. 408.
- [75] J. Gaudiakas, R. G. Haire, and J. Fuger, Thermodynamics of lanthanide and actinide perovskite-type oxides IV. Molar enthalpies of formation of MM' O<sub>3</sub> (M = Ba or Sr, M' = Ce, Tb, or Am) compounds, *J. Chem. Thermodyn.* **22**, 577 (1990).
- [76] L. R. Morss, Thermochemical regularities among lanthanide and actinide oxides, *J. Less-Common. Met.* **93**, 301 (1983).
- [77] P. G. Sundell, M. E. Björketun, and G. Wahnström, Thermodynamics of doping and vacancy formation in BaZrO<sub>3</sub>

- perovskite oxide from density functional calculations, *Phys. Rev. B: Condens. Matter* **73**, 104112 (2006).
- [78] J.-R. Martinez, C. E. Mohn, S. Stølen, and R. Søndergaard, What can a “quantum black-box” do for the inorganic thermochemist?, *Phys. Chem. Chem. Phys.* **8**, 2036 (2006).
- [79] L. J. Sham and M. Schlüter, Density-Functional Theory of the Energy Gap, *Phys. Rev. Lett.* **51**, 1888 (1983).
- [80] A. J. Cohen, P. Mori-Sánchez, and W. Yang, Fractional charge perspective on the bandgap in density-functional theory, *Phys. Rev. B* **77**, 115123 (2008).
- [81] P. Mori-Sánchez, A. J. Cohen, and W. Yang, Localization and Delocalization Errors in Density Functional Theory and Implications for Band-gap Prediction, *Phys. Rev. Lett.* **100**, 146401 (2008).
- [82] R. M. Martin, *Electronic Structure: Basic Theory and Practical Methods* (Cambridge University Press, Cambridge, 2004).
- [83] M. S. Hybertsen and S. G. Louie, Electron correlation in semiconductors and insulators: Band gaps and quasiparticle energies, *Phys. Rev. B* **34**, 5390 (1986).
- [84] F. Tran and P. Blaha, Accurate Band Gaps of Semiconductors and Insulators with a Semilocal Exchange-correlation Potential, *Phys. Rev. Lett.* **102**, 226401 (2009).
- [85] M. Shishkin and G. Kresse, Self-consistent GW calculations for semiconductors and insulators, *Phys. Rev. B* **75**, 235102 (2007).
- [86] S.-H. Wei and A. Zunger, Band offsets and optical bowings of chalcopyrites and Zn-based II-VI alloys, *J. Appl. Phys.* **78**, 3846 (1995).
- [87] P. G. Moses and C. G. Van deWalle, Band bowing and band alignment in InGaN alloys, *Appl. Phys. Lett.* **96**, 021908 (2010).
- [88] C. G. Van de Walle and R. M. Martin, Theoretical calculations of heterojunction discontinuities in the Si/Ge system, *Phys. Rev. B* **34**, 5621 (1986).
- [89] A. Franciosi and C. G. Van de Walle, Heterojunction band offset engineering, *Surf. Sci. Rep.* **25**, 1 (1996).
- [90] L. Köhler and G. Kresse, Density functional study of CO on Rh(111), *Phys. Rev. B* **70**, 165405 (2004).
- [91] S. Lizzit, A. Baraldi, A. Groso, K. Reuter, M. V. Ganduglia-Pirovano, C. Stampfl, M. Scheffler, M. Stichter, C. Keller, W. Wurth, and D. Menzel, Surface core level shifts of clean and oxygen covered Ru (0001), *Phys. Rev. B* **63**, 205419 (2001).
- [92] E. V. van Loef, Y. Wang, S. R. Miller, C. Brecher, W. H. Rhodes, G. Baldoni, S. Topping, H. Lingertat, V. K. Sarin, and K. S. Shah, Effect of microstructure on the radioluminescence and transparency of Ce-doped strontium hafnate ceramics, *Opt. Mater.* **33**, 84 (2010).
- [93] H. Retot, A. Bessiere, A. Kahn-Harari, and B. Viana, Synthesis and optical characterization of SrHfO<sub>3</sub>: Ce and SrZrO<sub>3</sub>: Ce nanoparticles, *Opt. Mater.* **30**, 1109 (2008).
- [94] T. Noguchi, T. Okubo, and O. Yonemochi, Reactions in the system ZrO<sub>2</sub>:SrO, *J. Am. Ceram. Soc.* **52**, 178 (1969).
- [95] J. K. Gleason, H. W. Olsen, and W. D. Turley, Pressure-induced luminescence quenching of terbium-doped oxide sulfides, *Inorg. Chem.* **32**, 639 (1993).
- [96] H. E. Hoefdraad, The charge-transfer absorption band of Eu<sup>3+</sup> in oxides, *J. Solid State Chem.* **15**, 175 (1975).
- [97] H. Yamamoto, M. Mikami, Y. Shimomura, and Y. Oguri, Host-to-activator energy transfer in a new blue-emitting phosphor SrHfO<sub>3</sub>: Tm<sup>3+</sup>, *J. Lumin.* **87**, 1079 (2000).
- [98] A. Dobrowolska and E. Zych, Forcing Eu<sup>3+</sup> into different positions in the BaHfO<sub>3</sub> host and its spectroscopic consequences, *Chem. Mater.* **22**, 4652 (2010).
- [99] S. K. Gupta, M. Mohapatra, V. Natarajan, and S. V. Godbole, Site-specific luminescence of Eu<sup>3+</sup> in gel-combustion-derived strontium zirconate perovskite nanophosphors, *J. Mater. Sci.* **47**, 3504 (2012).
- [100] S. Liu, X. Feng, Z. Zhou, M. Nikl, Y. Shi, and Y. Pan, Effect of Mg<sup>2+</sup> co-doping on the scintillation performance of LuAG:Ce ceramics, *Phys. Status Solidi* **8**, 105 (2014).
- [101] M. Nikl, V. Babin, J. Pejchal, V. V. Laguta, M. Buryi, J. A. Mares, K. Kamada, S. Kurosawa, A. Yoshikawa, D. Panek, and T. Parkman, The stable Ce<sup>4+</sup> center: A new tool to optimize Ce-doped oxide scintillators, *IEEE Trans. Nucl. Sci.* **63**, 433 (2016).
- [102] W. Chepraditkul, C. Wanarak, T. Szczesniak, M. Moszynski, V. Jary, A. Beitlerova, and M. Nikl, Comparison of absorption, luminescence and scintillation characteristics in Lu<sub>1.95</sub>Y<sub>0.05</sub>SiO<sub>5</sub>:Ce, Ca and Y<sub>2</sub>SiO<sub>5</sub>:Ce scintillators, *Opt. Mater.* **35**, 1679 (2013).
- [103] F. A. Kröger and H. J. Vink, *Solid State Physics – Advances in Research and Applications* (Academic Press, New York, 1957).
- [104] R. A. Davies, M. S. Islam, and J. D. Gale, Dopant and proton incorporation in perovskite-type zirconates, *Solid State Ion.* **126**, 323 (1999).
- [105] See Supplemental Material at <http://link.aps.org/supplemental/10.1103/PhysRevApplied.10.024026> for total and partial (Ce 4*f* and 5*d*) density of states for the two most stable Ce substitutional doping configurations in CaZrO<sub>3</sub>, SrHfO<sub>3</sub>, SrZrO<sub>3</sub>, BaHfO<sub>3</sub>, and BaZrO<sub>3</sub>.
- [106] B. J. Kennedy, C. J. Howard, and B. C. Chakoumakos, High-temperature phase transitions in SrHfO<sub>3</sub>, *Phys. Rev. B* **60**, 2972 (1999).
- [107] C. J. Howard, K. S. Knight, B. J. Kennedy, and E. H. Kisi, The structural phase transitions in strontium zirconate revisited, *J. Phys.: Condens. Matter* **12**, L677 (2000).
- [108] A. Ahtee, M. Ahtee, A. M. Glazer, and A. W. Hewat, The structure of orthorhombic SrZrO<sub>3</sub> by neutron powder diffraction, *Acta Crystallogr. B* **32**, 3243 (1976).